Department of Physics and Astronomy
University of Heidelberg

Master Thesis in Physics
submitted by

Marius Matthias Rimmler

born in Heidelberg (Germany)

2017

Operating a low-energy Electron Cooler at the Cryogenic Storage Ring CSR

This Master Thesis has been carried out by Marius Matthias Rimmler
at the
Max-Planck-Institut für Kernphysik
under the supervision of
Prof. Dr. Andreas Wolf

Operation eines niederenergetischen Elektronenkühlers am ultrakalten Speicherring CSR:

Diese Arbeit beschreibt die Vollendung des Einbaus und die erste Inbetriebnahme des niederenergetischen Elektronenkühlers am ultrakalten Speicherring CSR am Max-Planck-Institut für Kernphysik in Heidelberg. Das operative System des CSR Elektronenkühlers wurde aufgebaut und in Betrieb genommen. Dafür wurde eine Hochspannungsplattform gebaut, die die elektrostatischen optischen Elemente des Elektronenstrahls kontrolliert. Die zweite kryogene Strahlzeit (Frühjahr/Sommer 2017) des CSR wurde genutzt, um zum ersten Mal longitudinales Phasenraumkühlen in Form von Elektronenkühlung an einem elektrostatischen Speicherring zu zeigen. Desweiteren wurden Betatronoszillationen eines C_2^- Ionenstrahls untersucht, was es möglich machte die Injektion des CSRs zu optimieren. Das verbessert die Durchführbarkeit von Experimenten mit überlagerten Ionen- und Elektronenstrahlen. Dadurch ist der CSR Elektronenkühler bereit, um in der nächsten Strahlzeit quantendynamische Studien an dissoziativer Rekombination mit Elektronen in einer ultrakalten Umgebung durchzuführen.

Operating a low-energy Electron Cooler at the Cryogenic Storage Ring CSR:

This thesis reports on the finalization of the implementation and the first operation of the low-energy electron cooler at the cryogenic storage ring CSR at the Max-Planck-Institut für Kernphysik in Heidelberg. The operational system of the CSR electron cooler was set up and commissioned. For this purpose, a high-voltage platform has been build to control the electron beam optics. The second cryogenic beam time (spring/summer 2017) of the CSR was used to show for the first time longitudinal phase space cooling via electron cooling at an electrostatic storage ring. Furthermore, betatron oscillations of a C_2^- ion beam have been observed allowing optimizations of the CSR's injection which contributes to the feasibility of merged-beam experiments with electrons. With this, the CSR electron cooler is ready for quantum dynamical studies on dissociative electron recombination in a cryogenic environment in the next beam time.

Danksagung

Ich möchte allen danken, die das Entstehen dieser Arbeit möglich gemacht haben.

Allen voran danke ich *Andreas Wolf* für die willkommene Aufnahme in seine Arbeitsgruppe. Danke für interessante Diskussionen und hilfreiche Anmerkungen, jederzeit und besonders auch beim Entstehen dieser Arbeit. Vielen Dank dafür, dass ich im Rahmen meiner Arbeit an der ersten Strahlzeit des CSR Elektronenkühlers teilnehmen konnte.

Ich danke *Alexander Dorn* für die freundliche Übernahme der Zweitkorrektur dieser Arbeit.

Ein besonderer Dank gilt *Oldřich Novotný* für die umfangreiche und tolle Betreuung, das Korrekturlesen und vor allem für die Unterstützung während meiner Zeit am MPIK.

Ich möchte *Patrick Wilhelm* danken für die schöne, lustige und motivierende Zusammenarbeit am Elektronenkühler aber auch für die Zeit neben der Physik. Danke auch an *Sunny Saurabh* für die gemeinsame Zeit, vor allem auch auf der DPG Tagung in Mainz.

Ein großer Dank geht an alle Mitarbeiter im CSR Team, die mir mit Rat und Tat zur Seite standen. Besonders *Oliver Koschorreck*, *Rolf Epking*, *Manfred Grieser*, *Manfred König*, *Dirk Kaiser*, *Lukas Dengel* und *Karsten Stähle*.

Danke an *Stephen Vogel* und *Arno Becker* für die gemeinsame Arbeit im Ecool Team und die geteilte Erfahrung eurerseits.

Natürlich wäre diese Abschlussarbeit letzten Endes nie entstanden und das Physikstudium nie erfolgreich beendet worden ohne einige ganz besondere Menschen, die ich niemals missen möchte.

Danke an meine Mitbewohner und Freunde für die tolle gemeinsame Zeit.

Danke an meine Familie, meine Eltern *Sabine* und *Gerd* und meine Geschwister *Sophia* und *Niklas*, für alles.

Danke an meine Freundin *Christin* dafür, dass du an meiner Seite bist und immer an mich glaubst.

Contents

1 Introduction

All along the evolution of scientific research, its progress was sparked by the observation of extraterrestrial processes. This provoked an outstanding comprehension of complex phenomena in space and enlightened knowledge about plasma conditions and processes present in the interstellar medium (ISM). Quantum dynamical processes in this surrounding represent a fundamental building block of the ongoing chemical network which has great impact on the origin of our life.

In order to investigate these dynamics, physicists started building isolated laboratory systems that simulate special conditions in the according surroundings with the presence of particular reactants. This allows the probing of individual phenomena in a fully controllable environment.

A promising approach on such studies initiated already in the 19^{th} century with the birth of particle accelerators that allow to control and observe various atomic and nuclear interactions. In 1886, Goldstein discovered the first charged particle beam from a gas discharge lamp [Gol86]. Shortly after in 1894, Lenard succeeded in the extraction of a first accelerated electron beam [Len94]. With the emerging subject of nuclear physics by the discovery of the atomic nucleus by Rutherford in 1911 [Rut11], an accompanied breakthrough in accelerator physics led to the discovery of linear accelerators, cyclotrons and electrostatic accelerators in the 1920s and 1930s [Wid28, LE30, CW32]. The longing for higher energies resulted in the discovery of the synchrotron in 1945 by both Veksler and McMillan [Vek44, McM45]. Today, a combination of several synchrotron accelerators and a ring of superconducting magnets yields studies with 7 TeV proton-proton collisions and 574 TeV Pb-Pb collisions at LHC [Col06]. High energies in accelerator facilities brought forth the discovery and investigation of many elementary particles and important reactions.

Important reactions in natural plasmas, e.g. in cold parts of the ISM, rely on molecules that are primarily ionized by stellar and cosmic radiation and characterized by a very active chemical network with vanishing reaction barriers [Per15]. A convenient tool for such studies emerged through a branch of accelerator physics, i.e. storage rings. These devices feature an injection of desired atomic, molecular or cluster ions into a closed orbit. The ion species of interest can then circulate many times on a defined trajectory which results in a high duty cycle when repeatedly reacting with localized targets. In combination with a merged-beam section that superimposes atoms, electrons or photons to the stored ion beam, experiments at very low collision energies and a high resolution can be carried out when the velocity of the reactant beams is matched. The high laboratory frame energy and the electrostatic or magnetic optics together with a good vacuum and resulting minimized rest gas collisions, lead to a high signal to noise ratio of charge changing reactions on suited detectors. Long storage times coming from an ultra high vacuum provide a powerful starting point when it comes to the inherent complexity of molecules. The long lifetime of the molecule in the storage ring enables interaction of the molecule's dipole moment with the surrounding black body radiation field on large time scales. In a cold environment, molecules can then thermalize with its surrounding leading to a well-defined initial state preparation.

A merged-electron-beam line in an ion storage ring not only serves as an experimental platform for quantum dynamical processes such as recombination with electrons but also provides a valuable tool to attain a good quality of the stored ion beam. The merging of a monoenergetic, i.e. cold, continuously renewed and velocity-matched electron beam with the ions and subsequent interactions allow the ions to transfer a momentum to the electrons via Coulomb collisions. This results in a net cooling effect of the ion beam and is thus called electron cooling, that was described by Budker and Skrinskii [BS78] and developed since 1962.

The **C**ryogenic **S**torage **R**ing CSR at the Max-Planck-Institut für Kernphysik represents a perfectly suited device to study the astrochemical network in a simulated laboratory interstellar medium [VBB+16]. Its electrostatic architecture allows positively or negatively charged ions to circulate on a 35 m circumference in an 10 K environment at pressures below 10^{-14} mbar without mass dependence. Its first cryo-

genic operation in 2015 showed successful storage of ions for several thousands of seconds. Long storage times enabled stored molecules to radiatively relax towards their ro-vibrational ground state.

A second cryogenic beamtime is currently ongoing (spring/summer 2017) including the testing and operation of two new and unique experimental sections. A neutral beam line and a low-energy electron cooler for heavy ions, i.e. the CSR Electron Cooler, have been implemented.

In this thesis, much work has been done on the finalization of the implementation of the CSR electron cooler as well as on preparations towards its first operation. This required the concept and creation of a complete electronic circuit that is sending the electrons through the beam line by assigning appropriate potentials to the electron beam optics. A high-voltage platform was set up, equipped and operated for this purpose. After all, during the first operation of the CSR electron cooler, it was able to demonstrate electron cooling at an electrostatic storage ring for the first time including longitudinal phase space cooling to the ion space charge limit. In addition, this thesis contributed to a further understanding of the storage ring dynamics of the CSR by pointing out a useful technique to judge and optimize the quality of injection into the ring's closed orbit. This was done by investigations on the neutral beam profile of C_2 molecules resulting from autodetachment of C_2^-.

Outline

This thesis starts with a summary of the theory of stored particle beams and a basic introduction to the Cryogenic Storage Ring CSR in chapter 2. This is then followed by a more detailed explanation of the theory of electron cooling and a presentation of the CSR electron cooler in chapter 3. This chapter also reports on relevant experiments carried out in the electron cooler section with a special measurement scheme that motivates certain challenges on the operational system in chapter 4. This chapter first provides a detailed presentation of the electron beam line in terms of its electrostatic elements. Then, the challenges and the motivation of the manufacturing of a high voltage platform are introduced followed by a detailed explanation of the design and the working principle. The chapter closes with a report

on the operating CSR electron cooler. This is followed by observations of betatron oscillations from a neutral beam and optimizations of the injection in chapter 5. At the end, the thesis presents a Conclusion and an Outlook.

2 The Cryogenic Storage Ring CSR

This chapter treats the theoretical concepts for characterizing particles in a storage ring with special focus on the dynamics in the transversal degrees of freedom, which were investigated at the Cryogenic Storage Ring CSR in chapter 5 of this thesis. Additionally, this chapter provides information about the CSR design, the CSR ion production section and the installed and used detectors.

2.1 Stored particle beams

Storage of particles in storage ring facilities is based on the concept of manipulation of charged particle beams such that they can be confined to a closed orbit and circulate on a defined trajectory. In order to handle the particle beam, one uses the LORENTZ force

$$\vec{F_L} = q(\vec{E} + \vec{v} \times \vec{B}). \tag{2.1}$$

This counteracts the centripetal force $\vec{F_C}$, such that with

$$|\vec{F_L}| = |\vec{F_C}| = \frac{mv^2}{\rho_0} \tag{2.2}$$

a particle with mass m, charge q and velocity $\vec{v}$ is deflected by either an electric field $\vec{E}$ or a magnetic field $\vec{B}$ onto an orbit with curvature radius ρ_0.
A storage ring's architecture is either based on electrostatic or magnetic elements. With Equation 2.1 and Equation 2.2, this states

$$\rho_0 E = \frac{mv^2}{q} \tag{2.3}$$

for an electrostatic storage ring and

$$\rho_0 B = \frac{mv}{q} \tag{2.4}$$

for a magnetic storage ring, respectively. In Equation 2.3, one assumes that the electric field points towards the center of the curvature and is orthogonal to the particle propagation while in Equation 2.4, one assumes that $\vec{B}$ is always perpendicular to $\vec{v}$. Given a fixed curvature radius ρ_0 and a particle with charge q, one sees that in an electrostatic storage ring, the electric field strength scales with the kinetic energy of the particle while in a magnetic storage ring the magnetic field strength scales with the particle's momentum. This makes electrostatic storage ring facilities advantageous when switching between various ion species with different mass but unchanged kinetic energy. Then, the electrostatic elements can remain untouched. In addition, the maximal velocity of a storable particle with mass m in an electrostatic storage ring is larger since it scales with $v_{max} \propto m^{-1/2}$ while in a magnetic storage ring, this follows $v_{max} \propto m^{-1}$.

In the following treatment of the concepts and theory of stored particles, this thesis follows the discussion in [Hin08]. It should be noted that the upcoming formalism is identical for electrostatic and magnetic storage rings.

2.1.1 Coordinate system

When characterizing stored particles, one uses the standard coordinate system of accelerator physics that describes an arbitrary particle trajectory with respect to a well known *ideal particle* that orbits on the central path $\vec{r}_0(s)$, i.e. the *design orbit* of a storage ring. Here, s denotes the distance of an ideal particle from a fixed origin on the closed orbit which can be seen in the right of Figure 2.1. A random particle in a storage ring can be described by introducing a (x, y)-plane that is orthogonal to the ideal particle's direction of propagation $\vec{u}_s$ for all s, seen in Figure 2.1. Thus, the actual position of this particle is given by

$$\vec{r}(s) = \vec{r}_0(s) + x(s)\,\vec{u}_x(s) + y(s)\,\vec{u}_y(s), \tag{2.5}$$

where $x(s)$ and $y(s)$ are the radial and axial displacement from the central path, respectively, and referred to as transversal coordinates. Figure 2.1 shows a curvilinear coordinate system, which gives the line element

$$\mathrm{d}\vec{r} = \vec{u}_x \mathrm{d}x + \vec{u}_y \mathrm{d}y + \vec{u}_s\,(1 + hx)\,\mathrm{d}s, \tag{2.6}$$

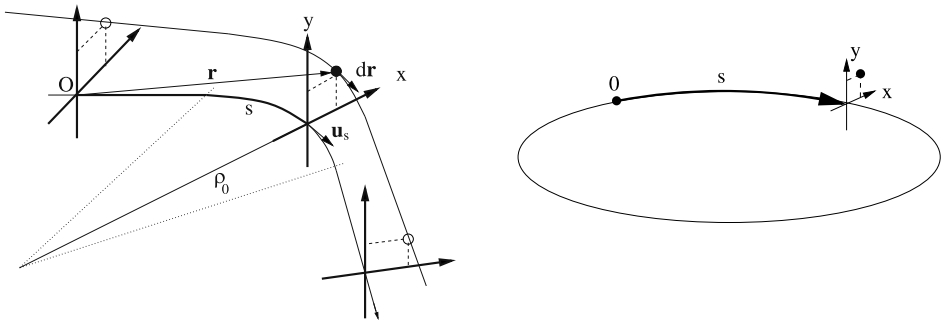

Figure 2.1: Co-moving coordinate system (x, y, s). The right side shows the coordinate system (x, y) that is moving on the circular design orbit s of the central particle. The left shows the deviation of a random particle from the central particle. ρ_0 is the curvature radius of the central particle's orbit. Taken from [Hin08].

at the position $\vec{r}(s)$. Here, $h = 1/\rho_0$ is the curvature of the particle's trajectory.

For the total definition of a particle, its six phase space coordinates (x, p_x, y, p_y, z, p_z) are required. For stored particles, this expression will be adapted by introducing the *divergences*

$$x' = \frac{\mathrm{d}x}{\mathrm{d}s}, \tag{2.7}$$

$$y' = \frac{\mathrm{d}y}{\mathrm{d}s}. \tag{2.8}$$

In linear approximation, one can show that $x' \propto p_x$ and $y' \propto p_y$. For the longitudinal degree of freedom, we introduce the longitudinal position displacement and the relative momentum uncertainty with respect to the central particle

$$l = -v_0 \left(t - t_0\right), \tag{2.9}$$

$$\delta = \frac{p - p_0}{p_0}, \tag{2.10}$$

respectively. In Equation 2.9, $\Delta t = t - t_0$ is the time difference between the actual particle and the central particle when passing the (x, y)-plane. This is projected to a longitudinal displacement by multiplication with the velocity v_0 of the central particle, i.e. $l > 0$ indicating a particle that is running ahead. With Equation 2.7 to Equation 2.10, one can entirely describe a single particle in phase space by the

six component vector

$$\vec{x}\,(s) = \begin{pmatrix} x_1 \\ x_2 \\ x_3 \\ x_4 \\ x_5 \\ x_6 \end{pmatrix} = \begin{pmatrix} x \\ x' \\ y \\ y' \\ l \\ \delta \end{pmatrix}. \tag{2.11}$$

2.1.2 Phase space

In subsection 2.1.1, we described single particles in a storage ring. If we think about a particle beam, we can consider a superposition of single particles represented by a beam intensity distribution, i.e. a density distribution $\rho\,(\vec{x})$ with the six dimensional argument $\vec{x}\,(s)$ shown in Equation 2.11. In order to study the transversal beam dynamics, it is important to consider the projections $\rho\,(x, x')$ and $\rho\,(y, y')$. These density distributions can be surrounded by an ellipse, i.e. the *phase space ellipse*. Considering the radial phase space ellipse[1], this can be represented by a 2-dimensional matrix

$$\sigma_x = \begin{pmatrix} \sigma_{11} & \sigma_{12} \\ \sigma_{12} & \sigma_{22} \end{pmatrix} \tag{2.12}$$

with symmetry $\sigma_{21} = \sigma_{12}$ and $\det \sigma_x > 0$, which has to fulfill $\vec{x}^{\mathrm{T}} \sigma_x^{-1} \vec{x} = 1$. Here, $\vec{x} = (x, x')$ is an arbitrary point on the edge of the ellipse. This gives the equation of the phase space ellipse

$$\sigma_{22} x^2 - 2\sigma_{12} x x' + \sigma_{11} x'^2 = \epsilon_x^2, \tag{2.13}$$

where $E_x = \pi \epsilon_x = \pi \sqrt{\det \sigma_x}$ is the surrounded area by the ellipse, which is called *emittance*. The radial phase space ellipse is visualized in the (x, x')-plane in Figure 2.2. It shows the maximal extend in $x'(x)$-direction $x'_{max}(x_{max})$ as well as the $x'(x)$-axis intersection $x'_{int}(x_{int})$. The area and angle of the ellipse in Figure 2.2 determine the properties of the beam. The angle indicates the correlation between the spatial displacement x and the divergence x' and the area represents the beam quality, i.e., the smaller the occupied area in phase space, the smaller the deviation

[1] analogous for the axial phase space ellipse.

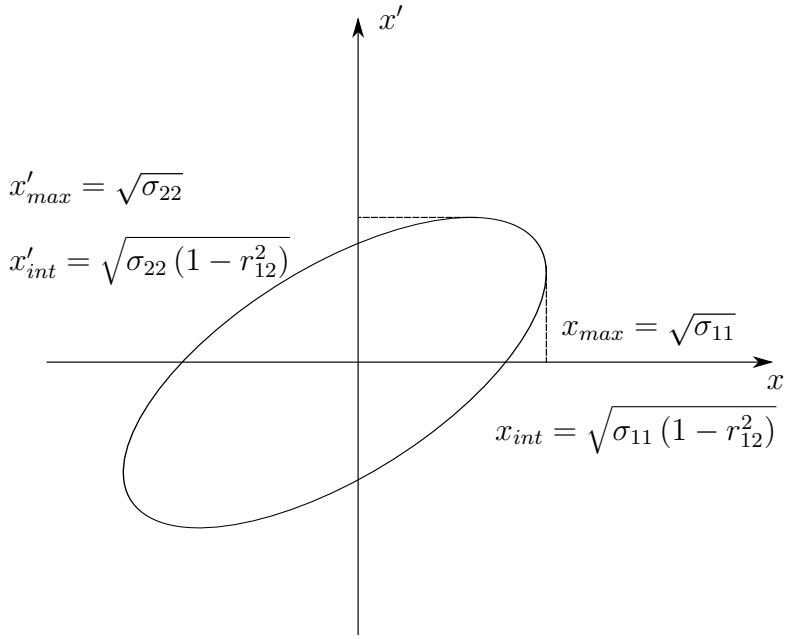

Figure 2.2: Phase space ellipse.

of random particles from the ideal particle.

The density distribution in phase space for the radial projection can be assumed to be a two-dimensional Gaussian distribution

$$\rho\left(\vec{x}\right) = \frac{1}{2\pi\epsilon_x} \exp\left(-\frac{1}{2}\vec{x}^{\mathrm{T}}\sigma_x^{-1}\vec{x}\right). \tag{2.14}$$

Together with the phase space ellipse that fulfills $\vec{x}^{\mathrm{T}}\sigma_x^{-1}\vec{x} = 1$, the emittance $E_x^{1\sigma}$ is representing an area of equal density surrounding 39.3% of the total intensity.

2.1.3 Transversal equations of motion

In Figure 2.1, a random particle at (x, y, s) experiences a radial acceleration $a_r = -\omega^2\left(\rho_0 + x\right)$, with the angular frequency $\omega = u_s/\rho_0$. Thus, with Equation 2.1, one can derive an expression for the dynamics in the (x, y)-plane that is parametrized with respect to an interval ds on the design orbit, which results in Hill's equations

[Hil86]:

$$\frac{\mathrm{d}^2 x}{\mathrm{d}s^2} + k_x(s)\, x = \frac{1}{\rho_0(s)} \frac{\Delta p}{p_0}, \tag{2.15}$$

$$\frac{\mathrm{d}^2 y}{\mathrm{d}s^2} + k_y(s)\, y = 0. \tag{2.16}$$

Here, the periodic functions $k_{x,y}(s) = k_{x,y}(s + C_0)$ give a measure for the focusing and defocusing, while $k_{x,y}(s) > 0$ represents a focusing and $k_{x,y}(s) < 0$ a defocusing force. Note that C_0 is the circumference of the ring. If we assume a neglectable dispersion from the bending in the (x, s) plane, i.e. $\Delta p/p_0 = 0$ for a monoenergetic beam, Equation 2.15 and Equation 2.16 both resemble the equation of a pseudoharmonic oscillator. The real-valued solutions of HILL'S differential equations describe the transversal particle motion in a storage ring which then follows the *betatron oscillations* [Ker41]

$$x(s) = a_x \sqrt{\beta_x(s)} \cos\left(\Psi_x(s) + \Psi_{0,x}\right), \tag{2.17}$$

$$y(s) = a_y \sqrt{\beta_y(s)} \cos\left(\Psi_y(s) + \Psi_{0,y}\right). \tag{2.18}$$

In these equations $a_{x,y}\sqrt{\beta_{x,y}(s)}$ represents the amplitude and $\Psi_{x,y}(s)$ is the phase of the oscillation, while Ψ_0 is an offset phase. The phase

$$\Psi_{x,y}(s) = \int_{s_0}^{s} \frac{\mathrm{d}s'}{\beta_{x,y}(s')} \tag{2.19}$$

is the betatron phase advance at s. The phase advance per revolution over 2π gives the number of betatron oscillations per revolution which is called *tune*

$$Q_{x,y} = \frac{1}{2\pi} \oint \frac{\mathrm{d}s'}{\beta_{x,y}(s')}. \tag{2.20}$$

A set of Q_x and Q_y gives the *working point* of a storage ring. It should be noted, that the tune values have to be non-integer numbers in order to perform storage of a beam. Integer tune values would cause resonances and result in strong betatron oscillations which makes storage impossible.

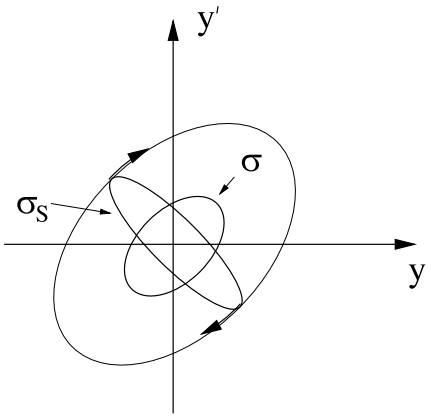

Figure 2.3: Mismatch of the machine ellipse σ and the beam (phase) ellipse σ_s. The betatron phase advance rotates the beam ellipse with each revolution, such that the beam ellipse covers a much larger area in phase space. Taken from [Hin08].

The betatron functions $\beta_{x,y}(s)$ are of central importance for a storage ring. It[2] is used to derive the *optical functions* of a storage ring

$$\alpha(s) = -\frac{1}{2}\beta'(s), \tag{2.21}$$

$$\gamma(s) = \frac{1 + (\beta'(s)/2)^2}{\beta(s)}. \tag{2.22}$$

The optical functions determine the accessible phase space in a storage ring characterized by the *machine ellipse*

$$\sigma = \epsilon \begin{pmatrix} \beta(s) & -\alpha(s) \\ -\alpha(s) & \gamma(s) \end{pmatrix}. \tag{2.23}$$

When injecting a particle beam into a storage ring, one tries to match the machine ellipse (Equation 2.23) and the phase ellipse (Equation 2.12). If this mismatches, the phase ellipse slowly approaches the shape of the machine ellipse which causes an increase of the emittance, shown in Figure 2.3. An optimization procedure for the quality of injection by correcting for a minimal amplitude of betatron oscillations will be presented later in this thesis by investigations of a C_2^- ion beam.

[2]We drop the index, since this derivation is valid for both x and y.

2.2 Design

2.2.1 Overview

Figure 2.4 shows a schematic overview of the Cryogenic Storage Ring CSR. The CSR is a quadratic electrostatic storage ring with 35.12 m circumference and four long free straight sections. It is designed for ion energies up to 300 keV per charge unit while its minimum design energy is 20 keV per charge unit.

A combination of an inner ion beam vacuum pipe (experimental vacuum) with a larger outer vacuum chamber (insulation vacuum) and a set of radiation shields support cryogenic operation of the CSR at temperatures of 10 K. This is enabled by a helium refrigerator system. With this, several helium tubes in the insulation vacuum distribute liquid and gaseous helium at temperatures of 2 K, 5 K, 40 K and 80 K through the CSR. During cryogenic operation of the CSR, cryopumps and vacuum chamber walls are cooled from the liquid 2 K line. The 40 K and 80 K lines cool two successive radiation shields in the insulation vacuum. When operating the CSR at room temperature, only the 5 K line is used for cooling of the cryopumps, the diagnostic system and the electron cooler. The cryopumps enable cryo-condensating of H_2 molecules which results in a room temperature equivalent pressure below 10^{-14} mbar in the beam line.

The ion optical elements are housed in the four symmetric rectangular corners (corner 1-4, counting from the injection and counterclockwise) and consist out of a combination of two electrostatic 6° deflectors and two 39° deflectors together with two focusing quadrupole doublets each. Single turn injection can be performed by fast switching of the 6° deflectors in corner 1, i.e. *kicker electrodes*.

Three of the four straight sections of the CSR (A,B,D) serve as platform for experiments while section (C) in Figure 2.4 is reserved for beam diagnostics. For detailed information about the diagnostic section, see [Vog16]. In this beam time, an ion-neutral merged-beam line in section (A) will be available [Gru16]. In section (B), an electron cooler for phase space cooling and electron-ion collision studies was implemented and put into operation during the work of this thesis which will be discussed

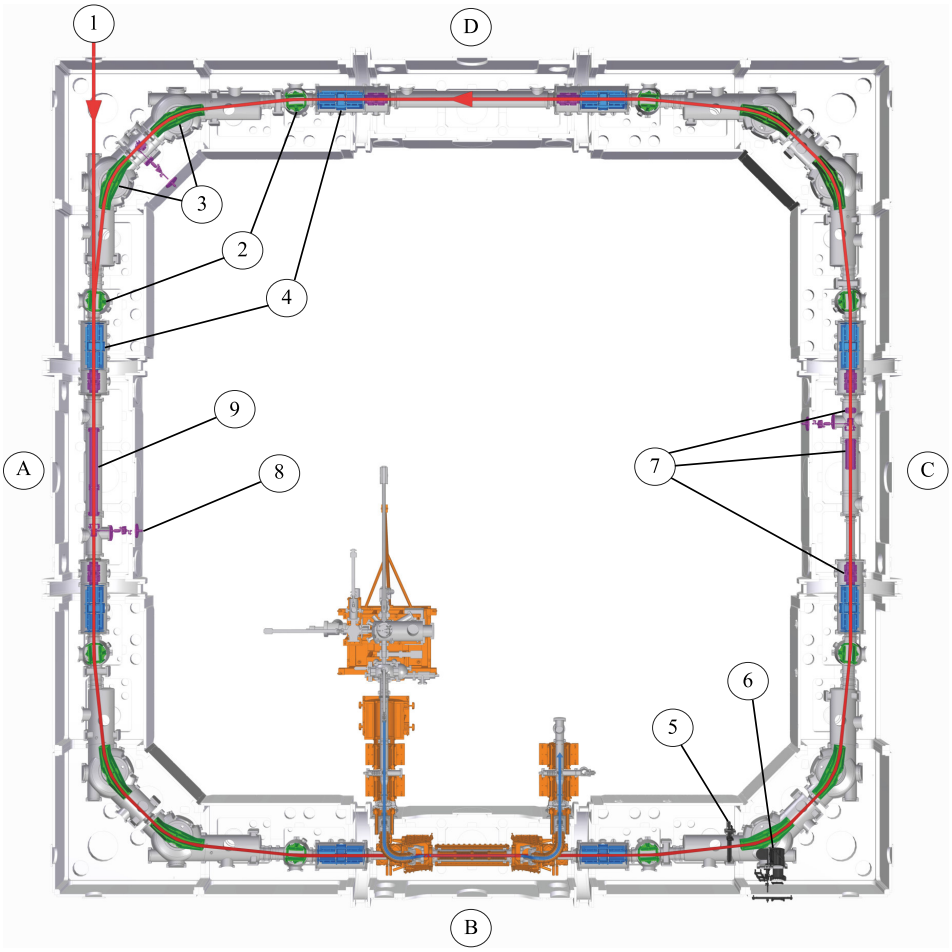

Figure 2.4: Model overview of the CSR. The ion beam (red) is injected at (1). It is confined to a closed orbit by four 90° corners, each consisting out of a pair of 6° deflectors (2), 39° deflectors (3) and two focusing quadrupole doublets (4). The CSR houses various tools for beam diagnostics in section (C) with current, SCHOTTKY, and position pick ups (7, counting from top). Three destructive beam-viewers are distributed to different locations in the beam line (8). The linear section (A) features a ion-neutral beam line and an RF bunching system (9). An electron cooler/target is implemented in section (B) for merged beam experiments with cold electrons while two detectors allow studies on both charged (5) and neutral reaction products (5+6). Section (D) will be equipped with a reaction microscope in future beam times.

in more detail in chapter 4. This section also serves as a platform for ion-photon experiments from laser induced reactions. A subsequent array of detectors at the end of this section allows studies on charged and neutral reaction products. Neutral product particles can be detected by the NICE, Neutral Imaging Cryogenic Environment, detector that is suited next to the 39° deflector in corner 3. The COMPACT, COld Movable PArticle CounTer, is a counting detector for electronic and photonic reactions with charged and neutral particle production. It is moveable across the beam line of CSR and will be discussed in more detail in subsection 2.2.3.

The fourth section (D) will provide a reaction microscope [WHG+06].

2.2.2 Ion production

The CSR facility comprises a versatile ion production section. Positively and negatively charged ions can be produced from a variety of ion sources sitting on a high voltage platform with energies up to 300 keV per charge unit. The ion source platform is coupled to the CSR via a transfer beam line introduced in [Gru16]. For the first beam time in 2017, the ion source platform contained a Metal Ion Sputter Source (MISS), a Penning source as well as an Electron Cyclotron Resonance (ECR) source. The first was used in the experiment performed with C_2^- in chapter 5. It can be used for the production of negative ions by using ionized Cs vapor. The Cs atoms come from an oven and after ionization on the hot surfaces, they are accelerated towards a target. The sputtering of the target releases ions, that can be extracted. By using different targets, one can access various ions, e.g. carbon ions from a carbon target.
In order to produce F^{6+} ions for the CSR electron cooler tests in section 4.2, we use the ECR source. This uses a hot plasma generated from a high energetic electron motion accelerated by the electric field of microwaves at the electron-cyclotron resonance frequency [AG81].

A combination of a 90° bending magnet right after the ion source on the platform with two 45° dipole magnets in the transfer line provides charge-to-mass separation of the ion beam. In order to supply a neutral beam to the CSR, a photodetachment section was installed prior to the injection into the CSR [Gru16]. Together with a

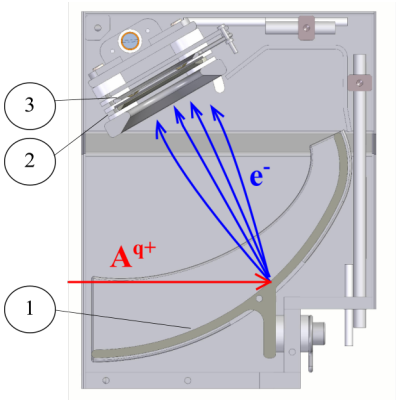

Figure 2.5: Cross sectional schematic view of the COMPACT detection principle. A particle A^{q+} hits the aluminum coated converter plate (1) and produces a number of secondary electrons e^-. The electrons are accelerated towards an MCP (2) and multiplied before they are detected at a subsequent anode plate (3). Taken from [Spr15].

second 60 keV source platform, the setup enables fast switching between neutral and charged particle beams.

2.2.3 CSR Detectors

As it was previously mentioned, the CSR setup benefits from two detector units located downstream in section (B) in Figure 2.4. This subsection will be dedicated mainly to the counting detector COMPACT which was used in this thesis in chapter 5. The NICE detector for neutral fragment imaging was unfortunately not available during this beam time. Its concept relies on a combination of a MCP, Multi-Channel Plate, to produce electron clouds from neutral particles together with a phosphor screen. Light spots on the phosphor screen indicate detection events and can be observed from the outside of the cryostat. This enables investigations on the energy balance in fragmentation reactions [Bec16].

The COMPACT detector was designed for the counting of reaction products in merged electron-ion beam experiments. Detailed information about the development and testing of this detector can be found in [Spr15]. Figure 2.5 and Figure 2.6 show the working principle and the position inside CSR of the COMPACT detector, respectively. The counting of particles works by the production of secondary

electrons at a converter plate backed by a MCP-anode stack. This sensor unit is sitting inside of a stainless steel housing with a sensor aperture of 20 mm width (x) and 50 mm height (y). The whole setup is movable across the beam line of the CSR along x via a translatioin stage such that it is possible to cover the beam path of various particles with different charge-to-mass ratio. The relative difference in charge-to-mass ratio η of daughter products (index d, reaction products) to parent products (index p, stored in the ring) can be given by

$$\eta = \frac{q_\mathrm{d}/m_\mathrm{d}}{q_\mathrm{p}/m_\mathrm{p}} - 1. \tag{2.24}$$

The theoretical range that is coverable by the COMPACT detector gives a limit of $-1.4 \leq \eta \leq 1.1$ which covers full neutralization ($\eta = -1$) as well as ionization to the double charge ($\eta = 1$) of the stored parent. A rotary drive provides access from the atmosphere side to the translation mechanics of the detector. One revolution of the drive proceeds the detector by 2 mm. Counting from the outermost position with respect to the center of the ring, the position of the neutral particle beam was found to be at 36 mm.

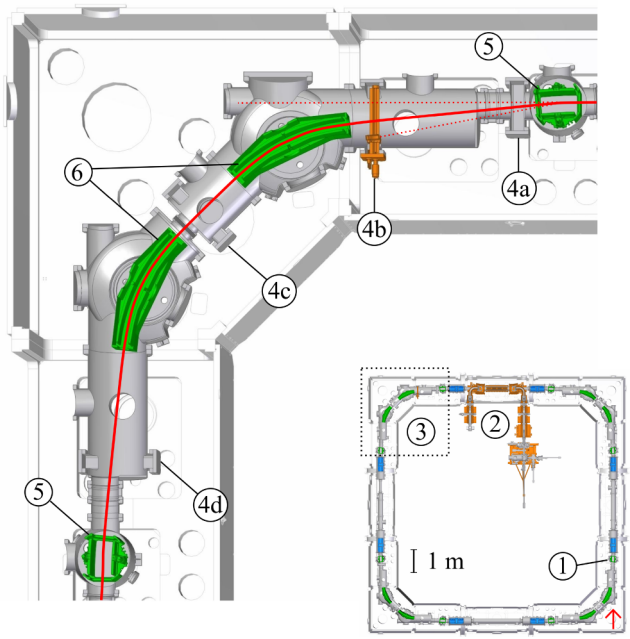

Figure 2.6: COMPACT detector position (4b) in the CSR. The detector is placed right after the first 6° deflector (5) in corner 3 (3), downstream the electron cooler section (2). The detector is moveable across the beamline via a translation stage. 1 - injection, 4a-4d - vacuum ports for installation of particle detectors, 6 - 39° deflectors. Taken from [Spr15].

3 The CSR Electron Cooler

This chapter covers the theoretical treatment of electron cooling and the technical realization of an electron cooler for ultra-low electron energies at the CSR. First, electron cooling will be presented as a useful tool for phase space cooling. This is followed by the calculation of the cooling force from the *binary collision model*. In the second section of this chapter the basic layout of the CSR electron cooler and applied peculiar techniques for ultra-low electron energy operation will be discussed. Finally, this chapter concludes with an overview of the experimental goals coming along with the CSR electron cooler which strongly motivates special requirements and challenges to the design of a high-voltage platform that was developed within this work in chapter 4.

3.1 Electron cooling

In subsection 2.1.2, we concluded that the occupied area of an ion beam in phase space shows an ellipse and is called beam emittance which represents a measurable quantity for the quality of the ion beam. This phase space ellipse changes its shape along the particle's orbit s but its area stays constant. The injected ion beam from the ion source has typically a large emittance. However, for experiments using the ion beam, especially in merged-beam configuration, a low emittance beam is preferred so that high energy-resolution measurements can be performed. According to Liouville's theorem, the beam emittance is constant in the absence of external forces. To overcome this limitation a velocity-matched, cold and continuously renewed electron beam can be superimposed to the ions. Coulomb interactions break the limitation of Liouville's theorem. At certain conditions this results in a low-emittance ion beam that is confined to a small diameter and divergence as well as a smaller momentum spread. This process is then called electron cooling [BS78].

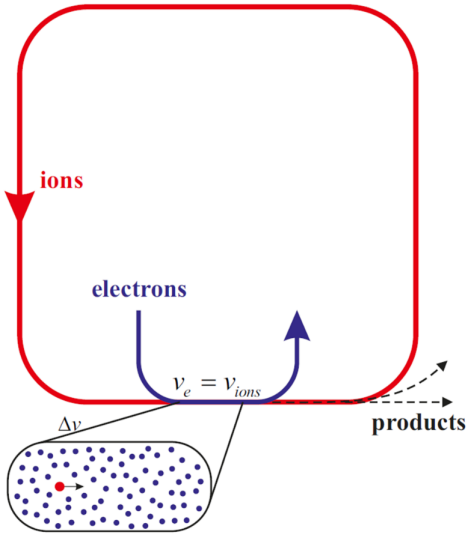

Figure 3.1: U-shaped electron cooler implementaion into an ion storage ring. Ions (red line) and electrons (blue line) are velocity-matched in the interaction region of the electron cooler.

The general schematic concept of the implementation of an electron cooler into an ion storage ring can be described by Figure 3.1. The ion beam circulates on its closed orbit and is merged with an electron beam in one of the free sections of the storage ring. The U-shaped design of the electron cooler allows merging and de-merging of the beams with a defined interaction region where phase space cooling can take place. Efficient phase space cooling requires the velocity-matching of both beams. Neutral products coming from recombination events in an electron-ion collision are no longer stored in the ring and are detectable in the corner downstream the electron cooler section.

3.1.1 Fokker-Planck Equation

From a theoretical point of view, the ion beam dynamics can be completely described by the phase space distribution function

$$\rho\left(\vec{r}, \vec{v}, t\right), \tag{3.1}$$

that assigns each individual particle its location in 6-dimensional phase space. Here, $\vec{r}$ is the location of the particle in position space and $\vec{v}$ is the 3-dimensional velocity

vector of the particle while t is an arbitrary point in time. In the presence of frictional processes, an expression for Equation 3.1 can be deduced from the FOKKER-PLANCK equation that will be presented in the following (following the derivation from [KT73]). Considering a finite probability $\Psi\left(\vec{v}-\Delta\vec{v},\Delta\vec{v}\right)$ for a particle with mass M, e.g. an ion, at velocity $\vec{v}-\Delta\vec{v}$ to undergo a collision, e.g. with an electron, and gather an additional kick $\Delta\vec{v}$ within $\mathrm{d}t$, one can assume that an arbitrary phase space function can be written as follows

$$\rho\left(\vec{r},\vec{v},t\right)=\int\rho\left(\vec{r},\vec{v}-\Delta\vec{v},t-\Delta t\right)\Psi\left(\vec{v}-\Delta\vec{v},\Delta\vec{v}\right)\mathrm{d}^3\Delta\vec{v}. \tag{3.2}$$

By a multidimensional Taylor expansion of Equation 3.2 to the second order and by performing the respective integration, one results in the FOKKER-PLANCK equation which simplifies in one dimension to

$$\frac{\partial\rho}{\partial t}=\frac{\partial}{\partial v}\left(-\rho\frac{F}{M}+\frac{\partial}{\partial v}\rho D\right), \tag{3.3}$$

where

$$D:=\frac{\langle(\Delta v)^2\rangle}{2\Delta t} \tag{3.4}$$

$$F:=M\frac{\langle\Delta v\rangle}{\Delta t} \tag{3.5}$$

are defined to be the *diffusion coefficient* and the *frictional force*, i.e. the heating contribution by multiple intrabeam scattering events of particles and the cooling contribution by an energy loss to external particles, respectively. Here, the brackets denote the averaging with $\Psi\left(v-\Delta v,\Delta v\right)$.

Equation 3.3 shows that electron-ion collisions represent indeed a useful method in order to access the phase space dynamics.

3.1.2 Binary Coulomb collisions

In order to further investigate electron cooling and to derive an appropriate expression for the frictional (cooling) force in Equation 3.5, one goes to the particle level and considers electron cooling as multiples of binary electron-ion collisions [Pot90],

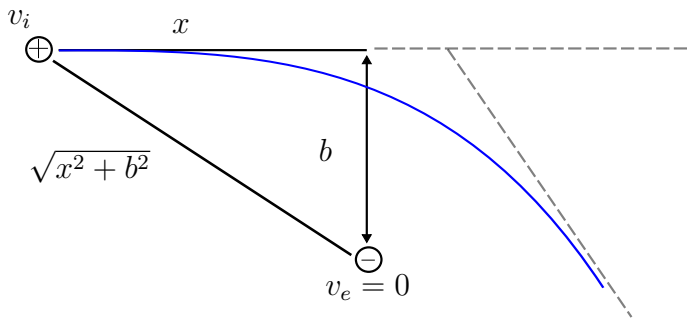

Figure 3.2: Binary electron-cation collision scheme. In the restframe of the electron ($v_e = 0$), an ion at a distance $\sqrt{x^2 + b^2}$ and with velocity v_i scatters off the electron and transfers a momentum to the electron. Here b denotes the impact parameter.

which is shown in Figure 3.2. In the restframe of the electrons, i.e. $v_e = 0$, the ions experience a non-zero velocity v_i. The two charged particles interact via COULOMB interaction, i.e. the COULOMB force F_{Coul}. The ion, with positive charge Ze, sees an attractive electrostatic potential from the electron charge $-e$ and scatters off the electron by RUTHERFORD scattering. Therefore the ion transfers a momentum

$$\Delta p = \int_{-\infty}^{\infty} F_{\text{Coul}} \mathrm{d}t = \frac{2Ze^2}{4\pi\epsilon_0 v_i b} \tag{3.6}$$

to the electron. When integrating over all times, one only considers a transversal momentum transfer in this scenario. Here, ϵ_0 is the vacuum permittivity and b is the impact parameter which is defined to be the closest distance between the two particles in Figure 3.2 when there would be no interaction. The corresponding energy transfer of the ion to the electron with mass m_e is

$$\Delta E\,(b) = \frac{-\,(\Delta p)^2}{2m_e}. \tag{3.7}$$

From Equation 3.6, this is inversely proportional to the square of the velocity of the ions v_i.

Multiple binary electron-ion collisions can be represented by an ion flying through a homogenously distributed cloud of electrons with density n_e in Figure 3.3. By multiplying Equation 3.7 with the linear electron density $N_e\,(b)$ and by integrating over the possible range of impact paramters, the energy loss of the ion per traveling

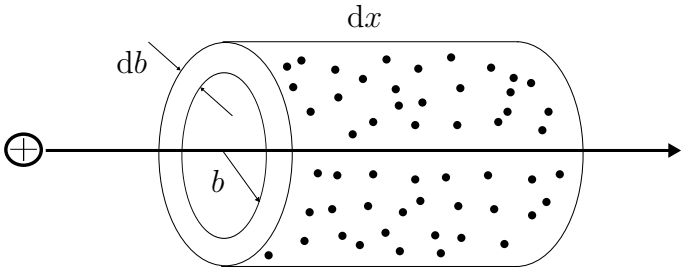

Figure 3.3: An ion travels through an electron cloud with electron density n_e and a linear electron density $N_e(b) = n_e 2\pi b \mathrm{d}b$.

distance $\mathrm{d}x$ can be calculated to be

$$\frac{\mathrm{d}E}{\mathrm{d}x} = 2\pi \int_0^\infty n_e b \Delta E(b)\, \mathrm{d}b = -\frac{4\pi Z^2 e^4}{(4\pi\epsilon_0)^2 m_e v_i^2} n_e \int_0^\infty \frac{\mathrm{d}b}{b}. \tag{3.8}$$

This expression can be interpreted as if the ion would receive a certain recoil that opposes its initial direction of motion. Therefore $F := \mathrm{d}E/\mathrm{d}x$ from Equation 3.8 can be defined as a cooling force F that lowers the initial energy of the ions in the frame of the electrons.

By introducing the COULOMB logarithm $L_\mathrm{C} = \int_{b_\mathrm{min}}^{b_\mathrm{max}} \mathrm{d}b/b$ with suitable cut-off impact parameters b_min, b_max, one can overcome the logarithmic divergence in Equation 3.8, when integrating from zero to an infinty. This results in

$$\vec{F}(\vec{v}_i) = \frac{\mathrm{d}E}{\mathrm{d}x}\frac{\vec{v}_i}{|\vec{v}_i|} = -\frac{4\pi Z^2 e^4}{(4\pi\epsilon_0)^2 m_e v_i^2} n_e L_\mathrm{C} \frac{\vec{v}_i}{|\vec{v}_i|}. \tag{3.9}$$

Appropriate values for b_min, b_max can be approximated. In absence of an external field, the DEBYE screening radius λ_D [Spi62] can be chosen as an upper limitation of the impact parameter

$$b_\mathrm{max} = \lambda_\mathrm{D} := \sqrt{\frac{\epsilon_0 k_\mathrm{B} T_e}{n_e e^2}}. \tag{3.10}$$

This is defined to be the distance from a positive test charge in an electron gas with temperature T_e and density n_e, where the observed electrostatic force from the positive charge decayed to a $1/e$ fraction by screening due to the regrouping of electrons. Here, k_B is the BOLTZMANN constant.

From collisional kinematics in the binary collision model, the maximal momentum transfer from the ion to the electron is limited by the ion's total initial momentum. This results in a limitation of the minimal interparticle distance and therefore the minimal impact parameter can be derived to be

$$b_{\min} = \frac{Ze^2}{4\pi\epsilon_0 m_e v_i^2}. \tag{3.11}$$

So far the electron's thermal motion was neglected in the calculation of the cooling force in Equation 3.9. In reality however, the electrons obey a Maxwell-Boltzmann velocity distribution $f(\vec{v}_e)$ with a thermal velocity spread deviating from the restframe at $\langle|\vec{v}_e|\rangle = 0$ by

$$\sigma_{v_e} = \sqrt{\frac{2k_B T_e}{m_e}}. \tag{3.12}$$

and consequently,

$$f(\vec{v}_e) = \frac{1}{\pi^{3/2}\sigma_{v_e}^3} \exp\left(-\frac{(\vec{v}_e - \langle\vec{v}_e\rangle)^2}{\sigma_{v_e}^2}\right). \tag{3.13}$$

In the co-moving frame of an ion at $\vec{v}_i$, the electron now attains the relative velocities

$$\vec{u} := \vec{v}_e - \vec{v}_i \tag{3.14}$$

and Equation 3.9 results in a convolution [Pot90]

$$\vec{F}(\vec{v}_i) = \frac{4\pi Z^2 e^4}{(4\pi\epsilon_0)^2 m_e} n_e \int L_{\mathrm{C}}(\vec{v}_e - \vec{v}_i)\, f(\vec{v}_e)\, \frac{\vec{v}_e - \vec{v}_i}{|\vec{v}_e - \vec{v}_i|^3} \mathrm{d}^3 v_e. \tag{3.15}$$

This means individual recoils experienced by the ion from the electrons now sum up statistically to the cooling force that opposes the motion. Equation 3.15 can be calculated analytically. Figure 3.4 shows the frictional character of Equation 3.15. The ion experiences a counteracting force that scales linearly with increasing ion velocity in the regime of small ion velocities. Its extreme is at $v_i - \langle v_e\rangle = \pm\sigma_{v_e}$. In the regime of large ion velocities, the absolute value of the cooling force decreases with $F \propto 1/(v_i - \langle v_e\rangle)^2$ which comes from the antiproportional dependence of the Rutherford cross section on the square of the ion-electron relative velocity. In Figure 3.4, one can clearly see an influence of the electron temperature on the max-

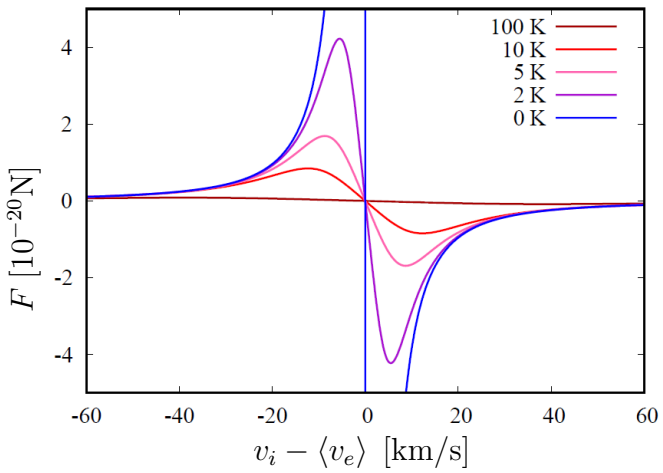

Figure 3.4: Cooling force (Equation 3.15) in one dimension for different electron temperatures T_e with respect to the ion's relative velocity. This was calculated by taking into account an ion with $Z = 1$ and an electron gas density $n_e = 10^6$ cm^{-3}. Taken and adapted from [Kra09].

imal value of the cooling force. The colder the electrons, the stronger the cooling force. This can be understood from a thermodynamical point of view when considering an electron-ion plasma with a temperature relaxation between the two species, i.e., the larger the temperature difference of the two species, the stronger the cooling effect on the hotter ions.

In analogy to the cooling force as a representative quantity for the cooling process of ions, the cooling time can be derived. With the ansatz

$$\frac{\mathrm{d}\vec{v}_i}{\mathrm{d}t} = \frac{\vec{F}\left(v_i\right)}{M}, \tag{3.16}$$

one observes an exponentially decaying relative ion velocity $v_i - \langle v_e \rangle$ in the regime of small ion velocities. The time constant of this process is the cooling time which follows [Spi62]:

$$\tau_{cool} \propto \frac{M T_e^{3/2}}{Z^2 n_e}. \tag{3.17}$$

Note that M is the ion mass.

Magnetic guiding field and thermal anisotropy

The guiding of the electron beam to the interaction region with the ions and included merging of the two beams takes place in the presence of a magnetic guiding field. This, in combination with the longitudinal acceleration of the electron beam, decouples the longitudinal and the transversal motion of the electrons and results in an anisotropic thermal velocity spread of the electrons [Wol92]. If $\perp = (x, y)$ denotes the transverse plane to the electron beam propagation axis indicated by $\| = z$, with $\sigma_{v_{e,x}} = \sigma_{v_{e,y}} = \sigma_{v_{e,\perp}}$, the electrons now follow the velocity distribution

$$f\left(\vec{v}_e\right) = \frac{1}{\pi^{3/2}\sigma_{v_{e,\perp}}^2 \sigma_{v_{e,\|}}} \exp\left(-\left(\frac{v_{e,\perp} - \langle v_{e,\perp}\rangle}{\sigma_{v_{e,\perp}}}\right)^2 - \left(\frac{v_{e,\|} - \langle v_{e,\|}\rangle}{\sigma_{v_{e,\|}}}\right)^2\right). \tag{3.18}$$

Here, $\sigma_{v_{e,\perp}}$ and $\sigma_{v_{e,\|}}$ denote the transversal and longitudinal thermal velocity spread, respectively. A quantitative measure for these can be given by the transversal and longitudinal temperature, i.e. $T_\perp$ and $T_\|$. Due to the "flattened" Maxwell-Boltzmann distribution in Equation 3.18, Equation 3.15 can no longer be calculated analytically.

In addition, in the presence of a magnetic field $\vec{B}$ the electrons are no longer free but confined to a spiral orbit such that they propagte on a spiral trajectory with the *cyclotron radius*

$$r_e = \frac{m_e v_\perp}{eB}, \tag{3.19}$$

where $v_\perp$ is the tangential velocity of the electron on the cyclotron orbit. This confined motion counteracts internal heating effects of the electron beam from Coulomb repulsion and makes electron cooling more efficient. A theoretical treatment of this was derived for the binary collision model by Derbenev and Skrinsky in [DS78].

3.2 Design

Efficient phase space cooling of ions with electrons requires matched average velocities of both particle species which can be seen in Figure 3.4. Consequently, this gives a requirement for the kinetic energy of the electrons E_{cool} for phase space cooling,

i.e.

$$E_{cool} = \frac{m_e}{2} \langle v_{e,\parallel} \rangle^2 = \frac{m_e}{M} E_i, \tag{3.20}$$

which is proportional to the ion energy E_i by the mass ratio m_e/M. Since the CSR was build for heavy-Ion studies up to a kinetic energy of 300 keV and electron cooling will be performed up to molecular ion masses of 160 u, this, together with Equation 3.20, results in a lower threshold for the electron energy of $\sim$ 1 eV. In combination with the goal of keeping the cooling times (Equation 3.17) short compared to the ion's lifetime, a device had to be build that can produce and handle low-energetic and cold electron beams with high densities in a cryogenic enviroment. The design of such an apparatus, namely the CSR electron cooler (*Ecool*), will be presented in the following subsection.

3.2.1 Overview

Figure 3.5 shows a model overview of the CSR Ecool. The electrons are produced in the room-temperature gun region of the electron cooler that is located inside the CSR (see Figure 2.4). The electrons are transported from a high magnetic field region through a lower magnetic field realized by copper-wound water cooled solenoids. From this it reaches the cryogenic part that is integrated into the CSR. There, a toroidal solenoid takes over the bending and merging of the electrons. The special design of the toroidal solenoid separates the bending and the merging process, which minimizes disturbance effects of the magnetic field on the ion beam [Sho12]. The merging procedure is supported by a set of vertical and horizontal racetrack merging coils. To further compensate effects on the ion trajectory, dipole correction coils right in front and at the end of the interaction region were implemented. The de-merging section of the cooler is mirror symmetric to the merging section. On a $\sim$ 0.8 m long interaction region, the electrons and the ions interact in the presence of a cylindrical magnetic field. Finally, the electrons are guided into the room-temperature collector part of the cooler where detailed analysis of the electron beam takes place.

All cryogenic coils are made out of High-Temperature Superconductor (HTS). This prevents possible heating effects from ohmic heat and provides a compact design due to the small cross section of the superconducting wires. These coils are all isolated

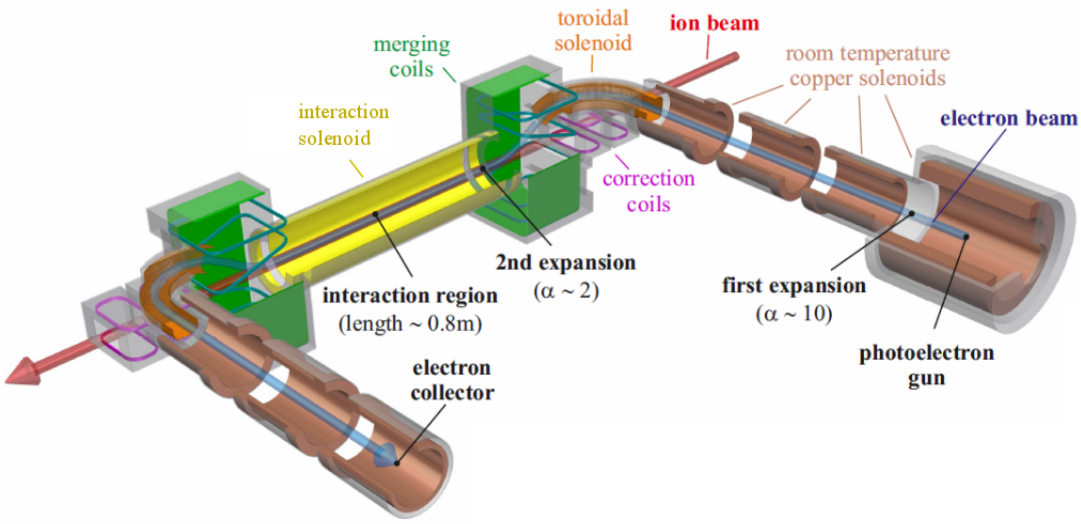

Figure 3.5: CSR Ecool design overview. Image courtesy of S.Vogel.

by superinsulation from other thermal regions of the cryogenic setup and cooled independently by a Low Pressure Cooling System (LPCS) that can be operated with neon [Sho12, Lio15] or helium. This allows operation of the CSR Ecool with other parts of the CSR either at cryogenic or at room temperature. In addition to the guiding, merging and compensation coils, there are several pairs of horizontal and vertical correction coils that are distributed all over the electron track to steer the electron beam.

The CSR Ecool features several different techniques that were implemented to provide a low-energetic, cold and dense electron beam. It benefits from a photocathode as a cold electron source as well as from an adiabatic magnetic transport region to further reduce the transverse temperature of the electron beam. Furthermore, it uses a decelerated electron beam in order to provide high electron densities at low energies. These features will be discussed in the following.

For a detailed study on the CSR electron cooler design, see [Vog16].

3.2.2 Cold electron beam production

When demanding an initially cold electron beam, one has to start encountering this challenge right at the electron source. Electrons are commonly produced when heating a thin metal wire to a temperature where the internal energy distribution exceeds the workfunction of the material $\Phi = E_{\mathrm{vac}} - E_{\mathrm{F}}$. Here, E_{vac} is the vacuum threshold while E_{F} is the Fermi energy. However, the extractable flux from such a thermionic cathode is given by the RICHARDSON law

$$J = A_G T_e^2 \exp\left(-\frac{\Phi}{k_{\mathrm{B}} T_e}\right) \tag{3.21}$$

and thus depends on the cathode temperature T_e. A_G is a material parameter of the cathode and k_{B} the BOLTZMANN constant. When aiming for high electron currents from thermionic cathodes, this is directly linked to a high electron temperature, e.g. 1200 K (∼100 meV energy spread) for compound metal oxides [Spr03]. Consequently, high current densities of cold electrons with an energy spread of the order of few meVs cannot be provided by thermocathodes. Therefore a photoelectron source was developed at the Electron Target of the Test Storage Ring at the Max-Planck-Institut für Kernphysik, which can produce electron beams while being cooled to liquid nitrogen temperatures resulting in an energy spread of 10 meV [Kra09]. Its working principle can be seen in Figure 3.6. The cathode material is a highly p-doped GaAs semiconductor layer. By irradiating this sample with a laser beam, electrons can be transferred from the valence band with energy E_{vb} into the conduction band E_{cb}. Here, the electrons thermalize towards liquid nitrogen temperature which is indicated by the sharp velocity distribution in Figure 3.6 and drift towards the cathode surface. This is coated with a CsO monolayer which lowers the vacuum threshold by ionisation effects and leads to a state of *negative electron affinity* (NEA) where the workfunction Φ is lower than the band splitting $E_{\mathrm{cb}} - E_{\mathrm{vb}}$ and electrons can escape into the continuum via tunneling without any further energy supply [SvL65]. However, a certain fraction of the electrons is reflected at the surface and this broadens the initially narrow energy distribution by a contribution that is almost of the order of the NEA [OAT00]. In pracitcal operation however, the electrons accumulate in front of the cathode surface and screen themselves by their own space charge potential V_{SC}. This results in a cut-off of the long Boltzmann-tail

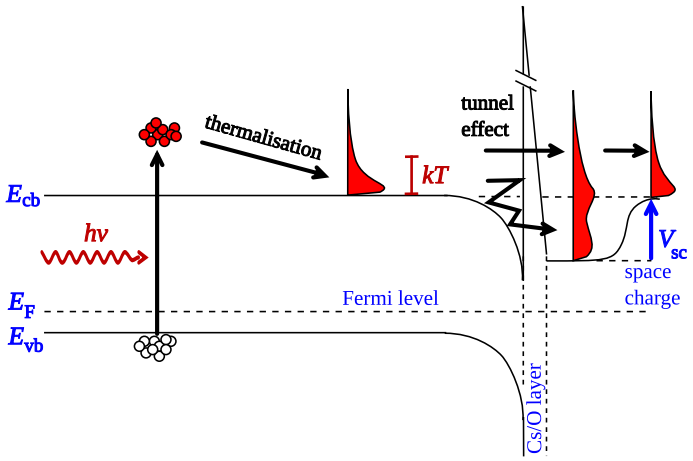

Figure 3.6: Cold electrons from a photocathode. A photon with energy $h\nu$ is absorbed by the GaAs sample and electrons are transferred from the valence band with energy E_{vb} into the conduction band with energy E_{cb}. The thermal energy spread of the electrons in the sample is indicated with kT. The electrons can tunnel through the surface thanks to a CsO monolayer that lowers the vacuum energy to a state of *negative electron affinity*. The electrons accumulate at the cathode surface and see their own space charge potential V_{SC}. In this space charge limited mode the emitted electron cloud obeys a small thermal energy spread. Taken from [Kra09].

and finally the extracted electron gas has an energy spread that is comparable to the thermal energy spread in the crystal which is of $k_{\mathrm{B}}T_{\perp} \approx 10$ meV when cooling to liquid nitrogen temperatures [OWS+04].

3.2.3 Adiabatic magnetic transport

If we transfer an electron longitudinally[1] from a region of high magnetic field strength into an area of low magnetic field strength, the electron is exposed to a magnetic field gradient $\mathrm{d}B/\mathrm{d}z < 0$. If the longitudinal variation of the magnetic field strength seen by the electron while performing one cyclotron spiral, i.e. within the *cyclotron length* $\lambda_c = 2\pi m_e v_{\parallel}/eB$, is very small compared to the total amplitude of the field B, then

$$\left|\frac{\mathrm{d}B}{\mathrm{d}z}\right| \frac{\lambda_c}{B} \ll 1 \tag{3.22}$$

and $|\mathrm{d}B/\mathrm{d}z|$ can be considered to be constant over the cross section of a particle orbit [PSG+96]. Considering an axially symmetric magnetic field, Equation 3.22 results in the adiabaticity of the magnetic moment [Dan93]:

$$\frac{\mathrm{d}\mu}{\mathrm{d}t} = \frac{\mathrm{d}\left(mv_{\perp}^2/2B\right)}{\mathrm{d}t} = \frac{\mathrm{d}\left(E_{\perp}/B\right)}{\mathrm{d}t} = 0. \tag{3.23}$$

If we now assign an initial transversal energy $E_{\perp,i}$ to an initial magnetic field B_i and ramp down B_i to B_f, then the final transversal energy follows

$$E_{\perp,f} = \frac{B_f}{B_i} E_{\perp,i} := \frac{E_{\perp,i}}{\alpha}, \tag{3.24}$$

with the expansion factor $\alpha = B_i/B_f$. In Figure 3.5, the electron source is embedded in a high magnetic field region, $B_i = 2500$ Gs, and electrons are adiabatically[2] transported to a low magnetic field, $B_{f,1} = 250$ Gs. This makes an expansion factor of $\alpha_1 = 10$. Then the electrons enter the cryogenic part where they see a solenoidal field of $B_{f,2} = 125$ Gs, which makes another $\alpha_2 = 2$, such that in total the transversal energy is reduced by a factor of 20 to $E_{\perp,f} = E_{\perp,i}/20$. With $k_B T_{\perp} \approx 10$ meV from the photocathode, this gives us access to transverse electron temperatures in the order of 0.5 meV.

[1] $\parallel$ shall be represented by the z coordinate.
[2] following Equation 3.22

3.2.4 Decelerating electron beam method

The challenge in producing low-energy electron beams at high densities is represented by the three-halves power law [Pot90]:

$$I = pU_{\text{ext}}^{3/2}. \tag{3.25}$$

The extractable current I is proportional to the extraction voltage U_{ext}, i.e. the potenital difference between the electron source and the electrodes in the beam line, to the power of three-halves and by means of the perveance[3] p. In the space charge limited mode, the electron density that can be generated from a source is limited by space charge effects not by the emissivity of the source. These effects can be pictured quantitatively by the perveance p, that is given by the electron gun geometry. Thus, at a given gun geometry, the density limitation can only be overcome by a deceleration of the electron beam. An expression for p in the cooler geometry can be derived from the cylindrical Poisson equation for ultra-low electron energy beams [Sho12]. Following this, one can get an expression for the perveance $p\,(U_{\text{SC}}/U_{\text{ext}})$ with respect to the ratio of the space charge potential U_{SC} to the extraction potential U_{ext} and derive a maximal pervence value at a given gun geometry. In the CSR, this gives $p_{\text{max}} \approx 5.4\,\mu\text{perv}$. Corresponding experiments with decelerated electron beams have shown that the CSR photocathode can reach an effective perveance $p = 4.1\,\mu\text{perv}$ which is slightly below the maximum perveance [Sho12]. For 1 eV electron beams and a standard gun perveance of $p = 0.58\,\mu\text{perv}$, this gives an enhancement of a factor of 7 for the current density[Sho12]. This allows to reach cooling times in the order of $\sim 100\,\text{s}$ which is well below the expected life time of the stored ion beam.

3.3 Electron cooler as a target

The CSR electron cooler Ecool not only provides a versatile tool in order to benefit from a low-emittance ion beam via electron cooling, but at the same time it also represents a platform to study electron-ion collision experiments in a cryogenic environment. The Ecool is thus serving as a cold electron target for various ion species,

[3] In units of $\text{A/V}^{3/2}$ or perv

which allows the probing of fundamental reactions at astrophysically relevant conditions. An environment of low black-body radiation and long storage times enable the preparation of well-defined initial states of ionic molecules prior to such probing experiments. This section starts with an introduction to the experimental goals of the Ecool and concludes with a basic explanation of the measurement procedure in merged-beam geometry. The latter is strongly linked to the upcoming requirements on the high voltage platform which was designed as described in chapter 4.

3.3.1 Experimental program

From astrophysical observations, one knows that molecular ions play a key role in astrochemical processes in the interstellar medium (ISM) [HvD09]. Investigations on the quantum dynamics of reactions involving molecules abundant in ISM consequently reveal valuable knowledge about the chemistry of interstellar clouds. These molecules can undergo collisions with free, low-energetic electrons which lead to fragmentation of the molecule into neutral products [LO08]. This process represents then recombination of an electron with a molecular cation and is therefore called *dissociative recombination* (DR). The CSR electron cooler represents a promising platform to study these kinds of reactions.

In DR, a molecular cation AB^+ captures a free electron and dissociates via a doubly excited repulsive state AB^{**} according to

$$AB^+ + e^- \rightarrow AB^{**} \rightarrow A + B + E_{KER}. \tag{3.26}$$

Here, E_{KER} is the kinetic energy release originating from the dissociation of the incident molecule. A major goal is probing this poorly understood mechanism experimentally with high resolution in order to provide fundamental contributions to theoretical modeling. The reaction 3.26 possesses several different decay channels resulting in a varying E_{KER} as well as neutral fragments A and B that can be generated in their ground state or in an excited state. An important parameter influencing this process is the collision energy of the electron-ion interaction. With our setup, combining a cryogenic heavy ion storage ring with a low-energy electron cooler and a coincidence-imaging fragment detector (NICE), we can examine the

reaction 3.26 under isolated conditions with defined parameters.

3.3.2 Measurement scheme

In the Ecool's straight section, we use the merged-beams technique to perform studies on collisional interactions between ions and electrons. This allows access to high energy resolution at the low collision energies reached by matching the velocities of the two reactant beams. Additionally, due to their high kinetic energy in the laboratory frame, the products, isotropically emitted in the center of mass frame, are directed into a cone pointing in the beam direction. This results in a high geometrical counting efficiency of the detector.

In the merged-electron-beam experiment that is carried out at the CSR, we benefit from a large electron beam that in many cases completely encloses the ion beam. The electron flux can then be considered constant and the reaction rate is independent of the overlap profile. This allows to approximate the cross section σ of an electron-ion interaction event from [PHDM99] to be

$$\sigma = \frac{R}{n_1 N_2 v_r}. \tag{3.27}$$

Here, R is the product rate, n_1 is the electron density and N_2 is the number of ions in the interaction region. $v_r = |v_1 - v_2|$ is the relative collision velocity, with v_1 being the electron velocity while v_2 is the ion velocity Due to the finite temperatures of the electron and ion beam, the particles obey a velocity distribution, resulting in a relative collision velocity spread. Taking this into account, we measure the *rate coefficient* of a reaction

$$\alpha = \langle \sigma v_r \rangle \,, \tag{3.28}$$

which is a convolution of the absolute reaction cross section σ and the relative collision velocity v_r. With simplified Equation 3.27, we get $\alpha = R/n_1 N_2$.

In order to perform electron-ion collision studies at non-zero collision energies while benefiting from the good quality of an electron cooled ion beam, one slightly detunes the electron energy E_e from the cooling energy E_{cool}. The latter is given by the velocity-matching in Equation 3.20. The electron-ion center-of-mass collision energy

is then given by the detuning [Lar97]:

$$E_d = \left(\sqrt{E_e} - \sqrt{E_{cool}}\right)^2. \tag{3.29}$$

This represents the kinetic energy of the electrons with respect to a target ion. The collision energy varies from Equation 3.29 due the finite electron beam temperature. The collision energy spread is governed by the electron velocity spread and given from [Mül99] by

$$\Delta E_{coll} \approx \sqrt{\left(\ln\left(2\right) k_{\mathrm{B}} T_{\perp}\right)^2 + 16 \ln\left(2\right) k_{\mathrm{B}} T_{\parallel} E_d}, \tag{3.30}$$

which strongly motivates a cold electron beam. It should be noted that the collision energy is independent of the ion mass due to the large mass difference of electrons and ions resulting in a reduced mass in the collision that is solely depending on the electron mass.

For measurement under ideal circumstances, one performs the electron energy detuning sufficiently fast in order to tune the collision energy to a desired value while also maintaining an electron cooled ion beam with low-emittance. This requires a fast switching of the electron energy E_e in Equation 3.29 in the interaction region of the ions and the electrons. This important criteria was taken into account while designing a high voltage platform for the electron optics potential, described in the following chapter.

4 Operational system of the CSR Electron Cooler

This chapter describes parts of the implementation and the first operation of the CSR electron cooler. In this thesis, the parameter range of desired electron energies and electron currents was used to design and manufacture a high-voltage system that enables a basic and also a complex time-dependent control of the electrostatic elements in the electron beam line. The electron cooler features various electrodes which guide the electrons as shortly presented in the beginning of the first section. A high-voltage platform was build up that is fitted to the needs of the CSR electron cooler. Its infrastructure and interior is described in subsection 4.1.1. The platform houses a power supply box that delivers potentials and allows the monitoring of currents at many important electrodes. Its design is discussed in subsection 4.1.2. In addition, the connections from the platform to the electrodes were completed which is shown in subsection 4.1.3. Finally, the second section of this chapter describes the first operation of the CSR electron cooler which achieved successful electron cooling of a F^{6+} ion beam.

4.1 The electron circuit

As indicated in the schematic overview of the electron cooler in Figure 3.5, the electrons are produced from a photocathode in the gun region. By putting the cathode setup on an negative potential with respect to ground, electrons can be extracted into vacuum. The kinetic energy of the electrons can be adjusted by putting several electrodes along the electron beam track on defined potentials with respect to the cathode. Figure 4.1 shows all electrodes in the CSR electron cooler schematically. This visualizes the electron track in one dimension. Figure 4.2 shows two potential distributions along the electron beam line which will be discussed in detail below. The electrons are produced in the gun region on the left. They fly through the in-

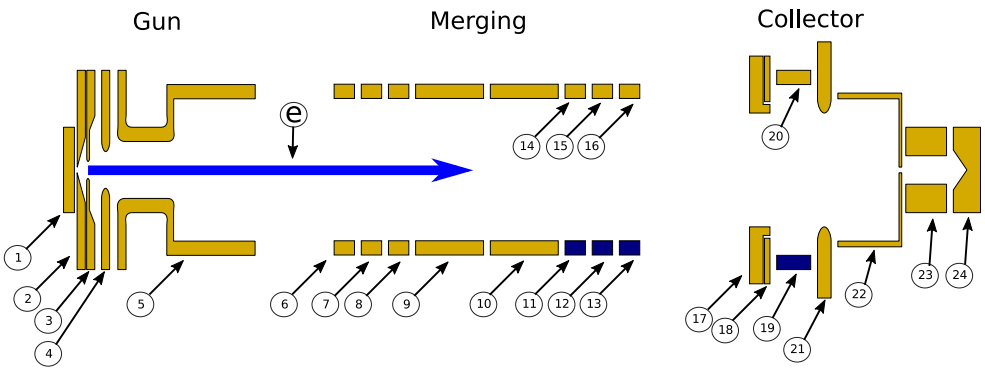

Figure 4.1: Schematic one-dimensional overview of the electrodes along the electron beam line. The propagation of the electrons from the gun region through the merging section to the subsequent collector section is indicated by the blue arrow. The electrons emerge from the cathode (1) through several electrodes: 2 - PIERCE electrode, 3+4 - Extraction electrodes, 5 - Drift electrode, 6-16 - Drift tube electrodes, 17 - First Repeller, 18 - Secondary electron collector, 19+20 - WIEN filter electrodes, 21 - Aperture, 22 - Main cup, 23 - Blocking electrode, 24 - Analyzer cup.

teraction region, where electron-ion interaction takes place ("merging") and finally enter the electron collector. All electrodes are spherically symmetric. Right after the production of the electrons at the cathode (1), they enter a set of electrodes in the gun section. The PIERCE electrode (2) serves for beam shaping purposes and can be set appropriately to obtain a homogeneous electron density distribution in the cross section of the beam [Spr03]. This is important for rate coefficient measurements presented in subsection 3.3.2. A pair of subsequent electrodes (3+4) extracts the electrons from the cathode surface. The next drift electrode (5), by the presence of a positive potential with respect to ground (see Figure 4.2), blocks the ions produced downstream of the beam line by electron collisions with the residual gas molecules. Such ions could experience a strong acceleration towards the cathode. The related high-energy ion bombardment of the cathode destroying its CsO layer and the GaAs bulk can result in a substantial degradation of the quantum efficiency [Kra09]. Coming from the electron gun, the electrons then enter the interaction region and pass eleven drift tube electrodes (6-16). Two centered and long electrodes (9+10) define the electron energy in the electron-ion interaction zone and three electrodes (6-8) right at the start as well as six electrodes (11-16) at the end of this region compensate for boundary effects. Different potential distributions can

be set as discussed below (Figure 4.2). The last six drift tube electrodes (11-16) are vertically separated such that with the application of an electric field gradient, one spills out ions from the rest gas that might be trapped in the space charge potential of the electrons which influences the efficiency of cooling.

Entering the collector region, the electrons are decelerated by a first repeller (17) before they hit the main cup (22), i.e. a FARADAY cup that collects most electrons and closes the electron circuit. A tiny fraction of the electron beam goes through a small pinhole in the main cup and a sweepable potential on the blocking electrode (23) in combination with an analyzer cup (24) allows studies on the longitudinal energy distribution of the electrons. By using an external transverse magnetic field, further upstream, one can also scan the electron beam over the pinhole in order to investigate the electron beam profile. Since not all electrons end up in either the main cup or the analyzer cup but some of them are reflected, i.e. *secondary electrons*, a WIEN filter was added to the set up with a pair of two WIEN filter electrodes (19+20) and a secondary electron collector electrode (18) [Loh15]. In combination with a set of HELMHOLTZ coils, backreflected and counterpropagating electrons now experience a drift to the edge of the beam line because of the superposition of electrically and magnetically induced forces. This, together with the relatively small kinetic energy of the electrons in the collector, minimizes the probability for electrons to propagate back to the gun region.

The potentials of the presented electrodes introduce a potential energy landscape to the electrons when propagating from the cathode to the collector. Depending on the desired electron energy in the interaction region, one either implements the deceleration configuration (see subsection 3.2.4) for low electron energies, which is shown in blue in Figure 4.2, or one can ground the drift tube electrodes for high electron energy operation, indicated in red in Figure 4.2.

Considering all electrodes along the electron track, we end up in 24 electrodes that require potentials to be individually controlled in terms of stability, flexibility and dynamic adjustement. A concept and its realization to manage these requirements will be presented in the following.

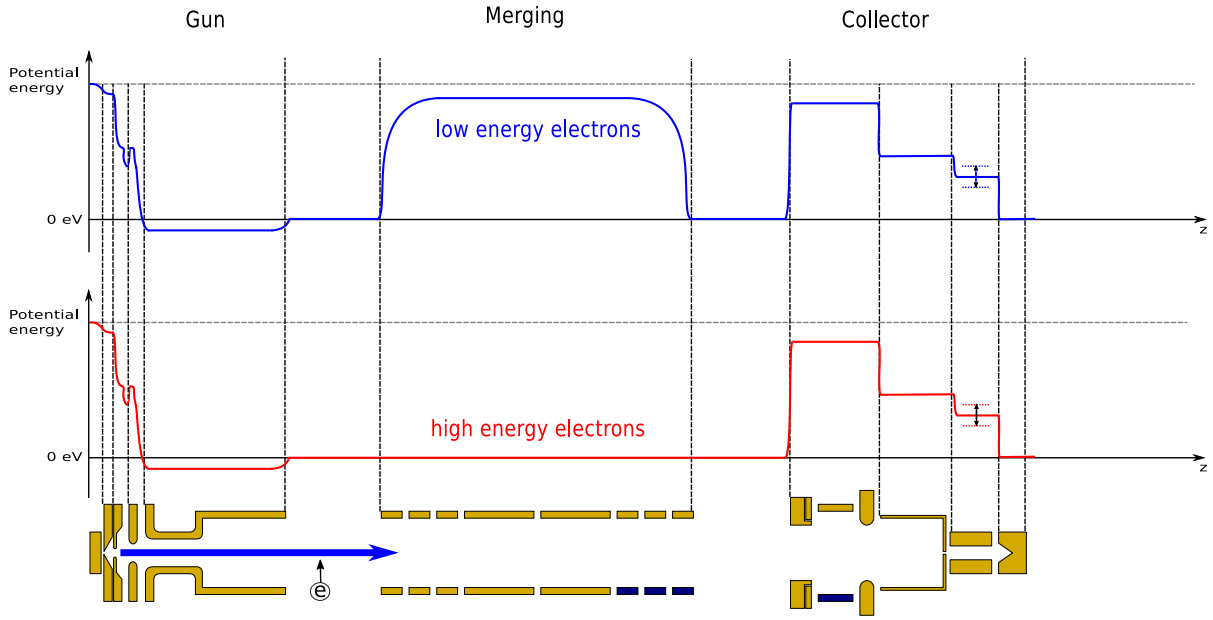

Figure 4.2: Schematic drawing of the potential energy landscape that is seen by the electron when passing the electrodes in the setup. The red curve shows the configuration for high energy electrons while the blue curve shows the deceleration configuration for low energy electrons. The electrons are produced from different cathode potentials that determine their maximal potential energy with respect to ground. In both modes of operation, the electron energy in the interaction zone is given by the potential difference between the cathode and the drift tubes.

4.1.1 The Ecool HV Platform

The operation of the CSR electron cooler sets various demands for an electronic system capable of dynamically controlling the electron motion through the electrode potentials.

Most importantly, the range of electron energies needs to be determined. In order to perform phase space cooling with a wide mass range of ion species, the electron energy has to be tuned appropriately to fulfill the velocity matching with the ion beam (Equation 3.20). As already discussed, considering heavy ions with a maximum mass of 160 u at 300 keV, we require laboratory-frame electron energies as low as 1 eV. However, for light ions, e.g. the proton with a mass of 1 u, 160 eV electron energy is needed. Furthermore, we want to deal with highly charged ions and access non-zero electron-ion collision energies by detuning the electron energy (see subsection 3.3.2). For setting higher collision energies in the interaction region, we consider electron energies up to 1 keV.

Generally, we can summarize the challenges to our system in the following:

1 Operate an electron beam with laboratory energies between 1 eV and 1 keV, i.e. a maximum cathode voltage of −1 kV with respect to the drift tube potential in the interaction zone. This makes high voltages and a related safety system necessary. Also, this large voltage range shall be covered without loss of energy resolution.

2 Fast detuning of the electron energy (ramping times of ∼1 ms)in the electron-ion interaction region (subsection 3.3.2) and deceleration of the electron beam for a dense low electron energy beam (subsection 3.2.4).

3 Remote control of all parameters. Implementation of measurement sequences via a Data Acquisition System.

These requirements have been fulfilled by implementing a high-voltage platform housing various power supplies. The platform potential directly sets the potential of the cathode. The potentials of all other electrodes are given by power supply units on the high-voltage platform, i.e. referenced to the platform potential. This

configuration is advantageous since most of the potentials do not need to be changed while the electron energy in the interaction zone is scanned by changing the cathode potential. In this case, simple power supplies with standard stabilities can be used on top of a highly stable power supply. An isolated 230 V (line power) source has to be implemented via an isolation transformer. In addition, all high voltages can be confined to a shielded housing of the platform with an interlock logic ensuring the safety of the operators.

With this configuration, one can implement the two modes of operation for either low or high electron energy. For low electron energy operation the platform voltage will be set to lower values (e.g. $-20\,\mathrm{V}$) and the drift tube electrodes will be lifted positively with respect to the platform voltage in order to decelerate the beam (see subsection 3.2.4). For high electron energies, the whole platform will be on a high potential (e.g. $-1\,\mathrm{kV}$), while the drift tube electrodes will be grounded, as we discussed earlier (see also Figure 4.2).

The connection scheme of the power supplies is shown in Figure 4.3. This figure shows an overview of the electronic logics of the high-voltage platform including all potentials, current measurements and control connections. Power supplies and special devices are framed and indicated by different colors.

On top of Figure 4.3, we see the well known electrode arrangement of the electron cooler. Ground potential is indicated at the bottom of the figure. A stable ($< 10\,\mathrm{ppm}$) ISEG EHQ 8205x power supply[1] ($-500\,\mathrm{V}/15\,\mathrm{mA}$) lifts the whole setup to the potential U_0. On top of this we have a Kepco BOP 100-1M power supply ($-100\,\mathrm{V}/1\,\mathrm{A}$) that lifts the platform and itself even further to an additional U_{kep}. The advantage of this additional offset is that it can be changed rather fast (slew rate $11\,\mathrm{V}/\mu\mathrm{s}$) in order to perform collision experiments with fast detuning of the electron energy.

The output of the stable ISEG power supply is connected to a high-voltage relay. An additional capacitance of $22\,\mu\mathrm{F}$ suppresses an AC voltage coupled in via the line-

[1] In a final configuration, this power supply will be replaced by a 1 kV power supply.

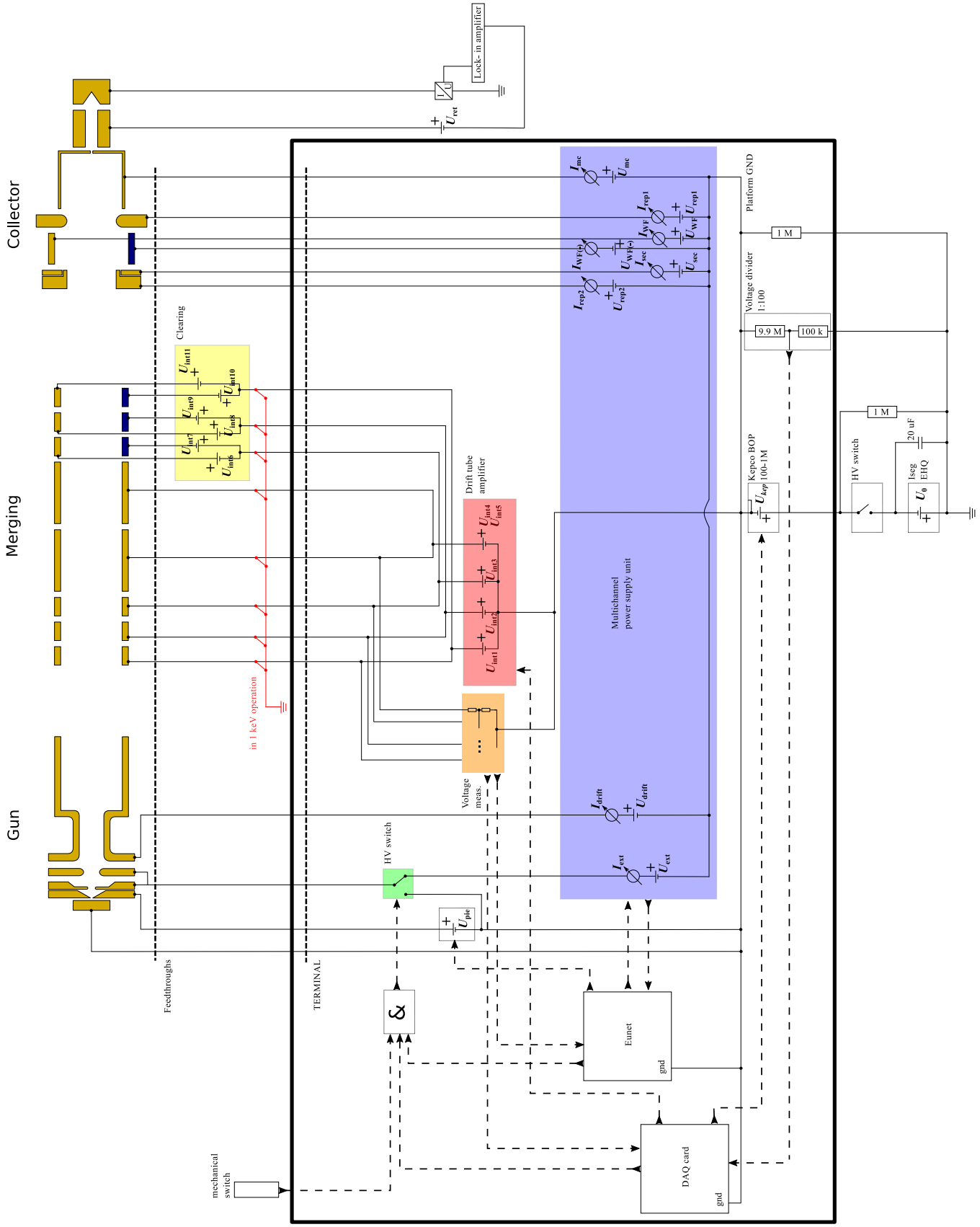

Figure 4.3: Total electronic circuit of the Ecool HV platform. Solid lines represent electronic connections. Dashed lines represent logic connections. The HV platform is indicated by the black frame.

power isolation transformer of the platform. The high-voltage relay is controlled by the interlock system and cuts the connection of the power supply to the platform during defined interlock scenarios. This has the advantage that switching of the ISEG power supply itself is not necessarily required and one can immediately proceed the operation after the closing of the switch. Right after the switch, we use a load resistance of 1 MΩ to stabilize the output. The applied platform (cathode) voltage can be read back via a 1:100 voltage divider (9.9 MΩ,100 kΩ) that supplies a 0 to 10 V output for platform voltages of 0 to (−)1 kV. An additional 1 MΩ load resistor discharges and stabilizes the platform.

The control system for the HV platform consists of a National Instruments USB 6343 DAQ card (16 Bit, 4 AO, 32 AI, 48 D I/O channels) and an EUNet control system that was developed at the Max-Planck-Institut für Kernphysik. Both of these systems are placed on the platform while the first one will be used for fast changes of parameters, e.g. drift tube voltages and platform offset voltage control (by Kepco PSU), whereas the latter will be used for slow or almost static parameters. Control and readout connections coming from and going to these control devices are indicated by the dashed lines, where the direction of the arrows shows output and input values, respectively. A USB to fiber converter is used to transport signals from a terminal computer to the DAQ card as well as an Ethernet to fiber converter to connect the EUNet system to the network.

An essential part of the platform is the multichannel power supply unit (MPSU, blue in Figure 4.3) that provides voltages to almost all electrodes. Its design features additional current measurements for all channels and will be discussed in subsection 4.1.2. The planning and setting up was carried out together with O. Koschorreck at the Max-Planck-Institut für Kernphysik.

In certain scenarios, e.g. performing background measurements without the electron beam, it is favorable to switch the electron beam on and off on a short timescale. Therefore, the power supply box provides a positive voltage to the extraction electrode, which is going into a fast high-voltage Behlke switch (green in Figure 4.3). It was designed to perform switching of up to 2 kV in the ms time scale with rise and fall times in the µs range [Spr03]. This combination allows fast switching between

electron beam on and off, where the extraction voltage is switched between positive and near-zero values with respect to the platform (cathode). The switching is controlled by a TTL signal that can come either from the USB DAQ card, the EUNet system or a mechanical switch, all signals being merged into a 3-channel AND-gate.

The PIERCE electrode can be covered directly by an analog output channel of the EUNet system due to its small voltage range (typically $\sim$2 V) [Spr03].

For the fast operation of the drift tube electrodes, a set of four amplifiers (red in Figure 4.3) is used to ramp up the electrodes symmetrically ($U_{\text{int1}} - U_{\text{int5}}$). Fast control is guaranteed by the USB DAQ card. In addition, the actual potentials of the four different drift tube voltages can be read back directly to the DAQ card by using a set of four high precision voltage dividers (orange in Figure 4.3). On top of the drift tube potentials, six individual clearing potentials (yellow in Figure 4.3, $U_{\text{int6}} - U_{\text{int11}}$) superimpose a gradient to the space charge potential of the electrons to spill out trapped ions. This power supply box will not be part of the HV platform which makes it applicable for both low and high (drift tubes grounded) electron energy operation. It consists out of a battery box floating on the drift tube potential which allows the application of a tuneable gradient potential to the clearing electrodes.

Additonally, the electronic circuit of the electron cooler collector is equipped with a retarding field analyzer section presented in Figure 4.2 and operated at previous electron cooler experiments by [Spr03]. With this section one can perform longitudinal energy distribution measurements by using a voltage to current converter at the analyzer cup to measure the electron current as a function of the retarding potential applied directly in front of this cup. Such that the integrated current $I(U_{ret}) = \int_{U_{ret}}^{\infty} f(U)\,\mathrm{d}U$ is measured to draw conclusions on the electron energy distribution function $f(U)$[2]. The setup benefits from the usage of a Lock-in amplifier that gives direct access to the derivative of the measured current signal from the Lock-in measurement and therefore to the energy distribution [Spr03]. This part is not included in the high-voltage platform.

[2]Note that $E_{kin} = Ue$.

It has to be mentioned that all outputs from the power supplies on the platform pass through a terminal plate that translates BNC and banana connectors to SHV plugs. The screening shield of the connected SHV cables has been interrupted at the side of this terminal plate so that grounding loops are avoided. These cables are then wired to the feedthroughs of the CSR electron cooler where the screen is defined to be the CSR ground potential.

Figure 4.4 shows a schematic drawing and a photograph of the front side of the Ecool HV platform. The cage is located at the very end of the electron beam track underneath the collector section in Figure 3.5. It provides two 19 inch racks with 14 rack units U height and 650 mm depth. The distribution of the housed devices was done accordingly to theses dimensions. Note that the USB DAQ card (1) and the drift tube amplifier box (2) were not implemented for the first basic testing of the CSR electron cooler. It should be mentioned that the NIM crate on the top right houses the HV switch for the extraction voltage, an optics-to-TTL receiver, a picoamperemeter and a floating amperemeter (counting from the left). The cage sits isolated on a plexiglas plate and is surrounded by a metal frame that prevents accidental touching of the high-voltage parts. The frame can be closed from the front side by a transparent door. The displayed connections follow the logics from Figure 4.3.

4.1.2 Multichannel power supply unit (MPSU)

As it was previously mentioned, the electronic circuit (Figure 4.3) required the design and the manufacturing of an 8-channel power supply box (MPSU, blue box in Figure 4.3) for the electrodes listed and specified with voltages in Table 4.1. Here, it should be noted that we refer to low energy electrons when want to go for the 1 eV operation as well as for electron energies up to 50 eV which allows us to cover most of the important molecules and atoms. For special cases of highly charged ions and non-zero electron-ion collision energies, we require high energy electrons with laboratory-frame energies up to 1 keV. To cover this energy range, we decided to have two power supply units in order to maintain a good stability. Additionally, a current measurement was implemented that is floating on top of the internal power supply and connected to the data acquisition system via an isolation

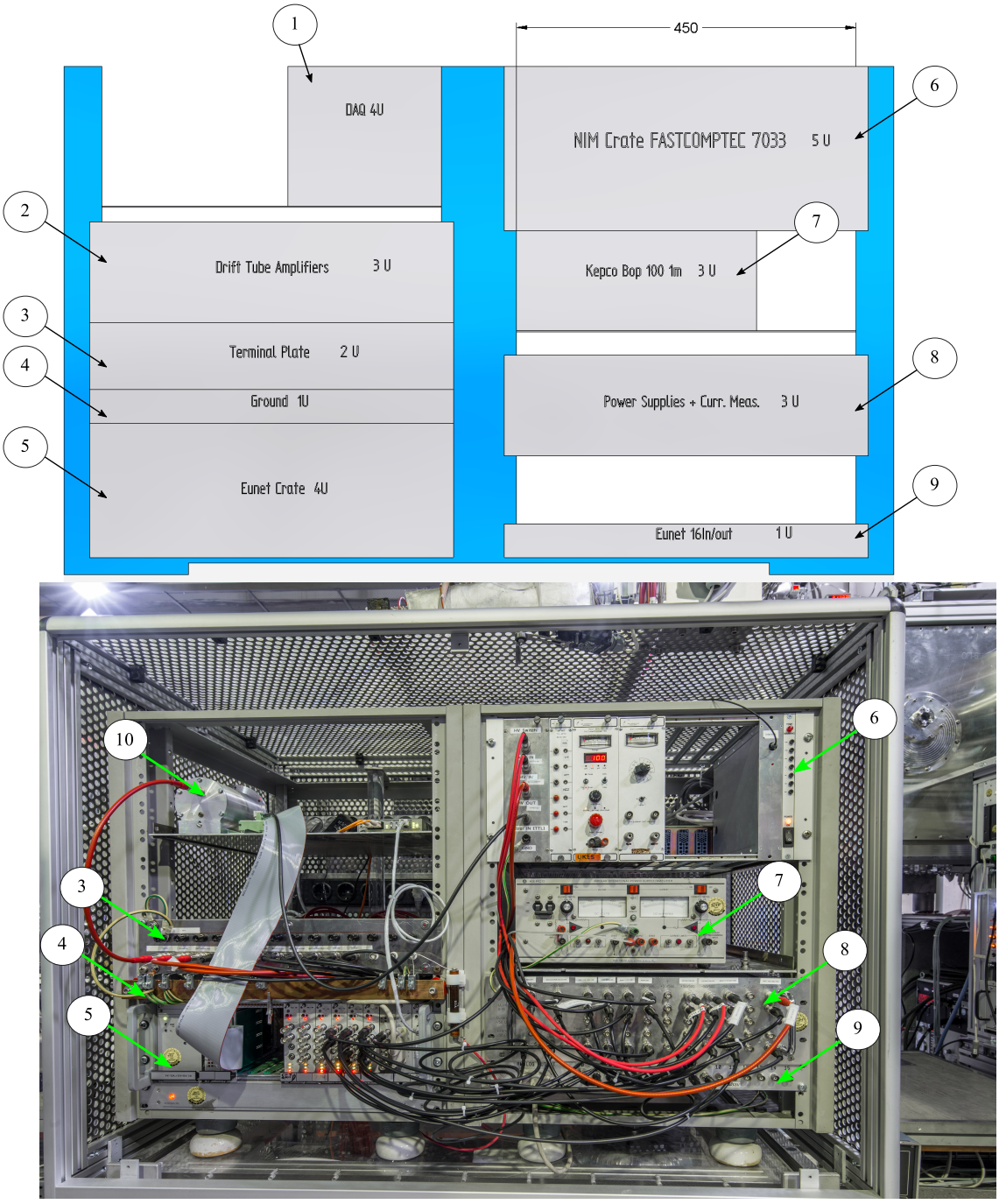

Figure 4.4: Schematic drawing and picture of the Ecool HV Platform cage. The included devices are labeled in the drawing. The corresponding height is given in rack units U. 1 - National Instruments USB 6343 DAQ card, 2 - Drift tube amplifier box (red and orange box in Figure 4.3), 3 - Terminal plate to the electrodes, 4 - Copper platform reference potential bar, 5 - EUNet system with included fan unit, 6 - 19 inch NIM crate , 7 - Bipolar power supply Kepco BOP 100-1M, 8 - MPSU (blue box in Figure 4.3), 9 - EUNet Breakout box (16 channel, AO), 10 - Voltage divider (1:100).

Electrode	high energy electrons	low energy electrons
Extraction on	0-500 V	0-50 V
Drift voltage	0-2000 V	0-500 V
First repeller	0-500 V	0-50 V
Wien filter top	0-500 V	0-50 V
Wien filter bottom	0-(-)500 V	0-(-)50 V
Secondary electron collector	0-500 V	0-50 V
Aperture	0-500 V	0-50 V
Main cup	0-500 V	0-50 V

Table 4.1: Chosen voltage ranges for all electrodes (except drift tubes, PIERCE electrode and analyzer section) in terms of voltages for both high and low electron energy operation.

amplifier. The current measurement is done by measuring the voltage drop over a resistor. The current measurements at two channels where we expect most electrons to impinge on the electrodes, i.e. the main cup and the secondary electron collector, are most critical for the data acquisition. Here, high precision and fast response (<1 ms) are required. Therefore the current measurements in these two channels were implemented by precision resistors and high-end isolation amplifiers. Also, an additional measurement output was provided to the fast control system. For the remaining channels, where the current measurement provides only orientational information, less precise electronic elements have been used.

Figure 4.5 shows the schematic logics of the two types of power supply units that were implemented into the MPSU. A detailed plan of the electronics of both of these units can be found in Figure A.1 and Figure A.2. In both layouts, one switches between a high-voltage ISEG BPS power supply (500 V/8 mA) or an operational amplifier OPA454 (50 V/50 mA) for high or low electron energy operation, respectively. The switching is done by a high-voltage relais that can be controlled by a TTL signal (e.g. from EUNet). Shortcutting the input (e.g. by an 50 ohm terminator) is equivalent to a TTL-low value, while open connector mimics the TTL-high value. The TTL-high value sets the small voltage range, while the TTL-low value sets the high voltage range. Also, the current range is adapted similarly by a second relais that

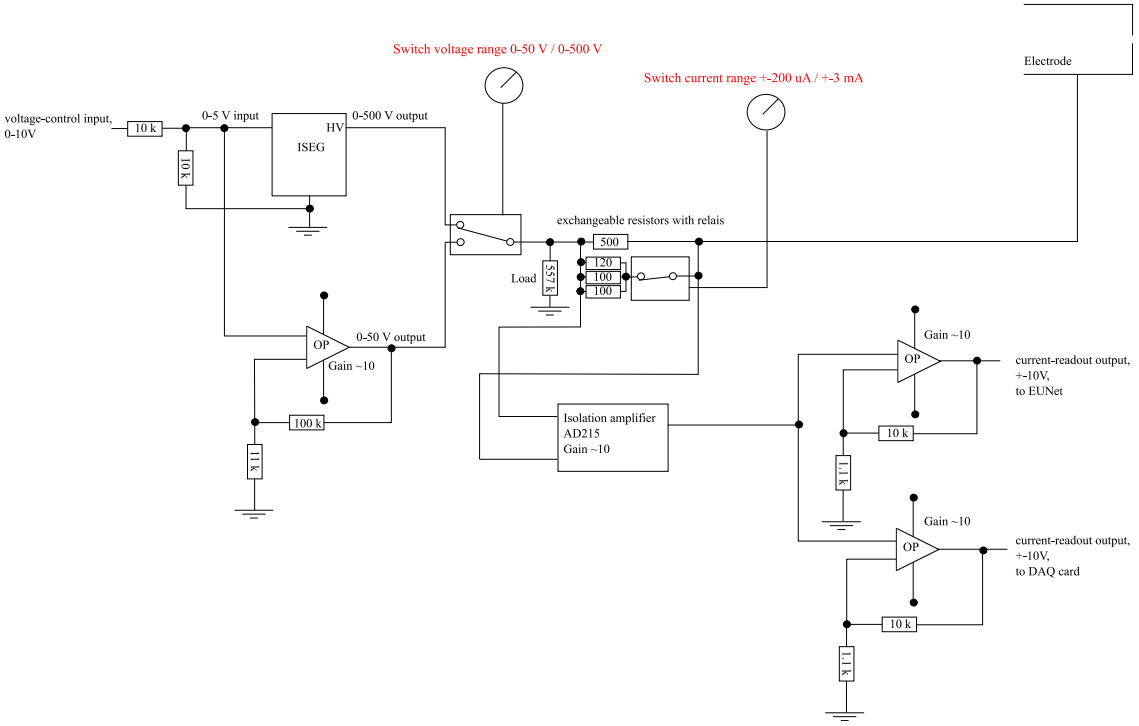

(a) Schematic logics of a precise power supply unit of the MPSU.

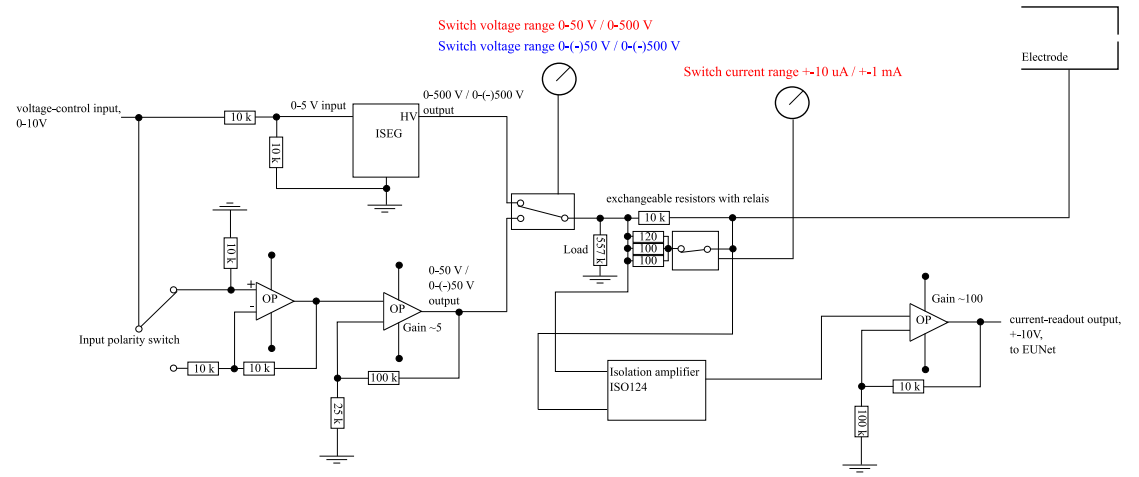

(b) Schematic logics of a bipolar power supply unit of the MPSU.

Figure 4.5: Power supply units

changes the measurement resistance (current sensitivity). Here, the TTL-high value sets the large current range, while the TTL-low value sets the small current range.

For low electron energies and small electron currents in Figure 4.5a, we operate with the 0 to 50 V operational amplifier (OP) and a 500 Ω measurement resistor on top, which gives at estimated maximal electron currents of 200 µA a voltage drop of 0.1 V on the resistor. For high electron energies, we operate 0 to 500 V from the ISEG module and we put 120 Ω, 100 Ω and another 100 Ω resistance all in parallel with the previous 500 Ω to get a 36 Ω resistance in total. With this and an estimated maximal electron current of 3 mA, we result again in 0.1 V drop over the resistor. This signal is floating and fed into an isolation amplifier AD215 (120 kHz full-power bandwidth). Here, we implement a voltage gain of a factor of 10. Together with two subsequent operational amplifiers as impedance converters and an additional gain of 10 we get a −10 to 10 V output signal for both the EUNet system as well as for the USB DAQ card.

For the regular power supply unit in Figure 4.5b, we use a different isolation amplifier ISO124 (50 kHz signal bandwidth) and only provide one measurement output. These units will be implemented when the current measurement is only required for diagnostic purposes, e.g. identification of electron beam misalignment by observing unexpected current on some electrodes. Therefore, we implement a 10 kΩ resistance to read out currents up to ±10 µA (±10 V on the output). This is switchable to 100 Ω when we want to measure currents in the 1 mA range. It should be mentioned that these regular power supply units were designed for bipolar operation[3] which is realized by switching an operational amplifier in Figure 4.5b that is inverting the input from the EUNet system.

13 of these power supply units were put into a 3U box, where we made 2 precise units and 11 bipolar units (9 positive, 2 negative) operational. This gives us some freedom for future configurations, while for now we operate 8 of these units. The front panel of this box features output signals for the electrodes, voltage-control input connections, range switching connections for both voltage and current and a

[3]The polarity has to be fixed before implementation of the module. The switching is done directly on the printed circuit board.

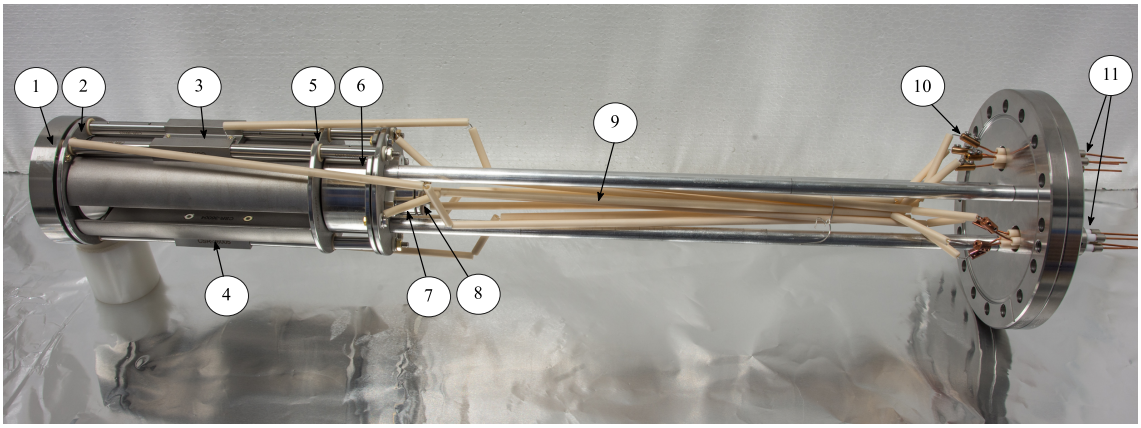

Figure 4.6: UHV parts of the Ecool Collector. This picture shows all electrodes in the collector section. Electrons are coming from the left side. 1 - Repeller electrode, 2 - Secondary electron collector, 3 - Wien filter top electrode, 4 - Wien filter bottom electrode, 5 - Aperture, 6 - Main cup, 7 - Blocking electrode, 8 - Analyzer cup, 9 - Silver coated aluminum wires with ceramic insulation, 10 - CuBe clamps, 11 - two 4-pin CF feedthroughs.

current-readout connection.

4.1.3 The collector

A detailed description of the design and the working principle of the electron collector section of the CSR electron cooler can be found in [Loh15], while the collector electrodes were also presented in the first section of this chapter. Within the scope of this thesis, all the electrodes in the collector section were wired to ultrahigh vacuum feedthroughs and guided to connectors on the atmospheric site. A photograph of the UHV parts of the electron collector right before mounting in the Ecool chamber is shown in Figure 4.6. Electrons enter the collector section from the left side in Figure 4.6 before the accumulate on the main cup (6). A combination of a Repeller electrode (1), a Secondary electron collector (2), two Wien filter electrodes (3+4) and an Aperture electrode prevents the production and the backstreaming of secondary electrons produced on the main cup. The Blocking electrode (7) together with the Analyzer cup (8) enables studies on the longitudinal energy distribution of the electorns. All electrodes are connected to a pair of CF feedthroughs (DN16CF-4Pin-Cu-6kV-Ceramtec 9871-08-CF) (11) by silver coated aluminum wires that are surrounded by baked-out ceramic insulation tube (9). The connection is done with

eight CuBe clamps (10). The whole setup was implemented into the vacuum of the collector side of the CSR electron cooler. Additionally, the copper pins on the atmospheric side were connected to teflon-insulated wires that are going to a set of SHV connectors.

The wiring of gun related and drift tube electrodes was realized in [Wei03] and [Vog16] respectively.

4.2 Operation of the CSR Electron Cooler

After completing the implementation of the CSR electron cooler, we were finally able to show successful operation in terms of electron cooling of a 1.35 MeV F^{6+} ion beam. By matching the electron velocity v_e and the ion velocity $v_i = f_0 C_0$, where $f_0 = 107.184\,\mathrm{kHz}$ is the revolution frequency of the ion and $C_0 = 35.12\,\mathrm{m}$ is the circumference of the ring, we calculate the cooling energy of the electrons to be $E_{cool} = m_e v_i^2/2 = 40.28\,\mathrm{eV}$. We operate the electron circuit in a simplified configuration, with the drift tube electrodes grounded. In this case, the electron energy is dominantly given by the cathode potential U_0 as

$$E_{cool} = -eU_0 + W_c - W_a - eU_{sc}, \tag{4.1}$$

corrected for the contact potentials of the various electrodes, represented by the workfunction of the cathode W_c and the anode (drift tube electrode) W_a, and for the space charge field U_{sc} built within the electron beam [KHS+92].

4.2.1 Observation of longitudinal phase space cooling

In the first electron cooling tests, we have observed the longitudinal cooling effect (along the ion beam propagation) on a bunched ion beam. In these tests the ion beam has been excited by an RF field applied on a dedicated electrode ([VBB+16], see Figure 2.4) at a frequency of $2f_0$. By the application of an RF voltage signal, with $f_{RF} = 2f_0$, one introduces an energy shift $\mathrm{d}E/\mathrm{d}t$ to the ions which varies with the phase ϕ or the ion position $s = -C_0\phi/2\pi h$ ($h = 2$), in Figure 4.7. *Synchronous*

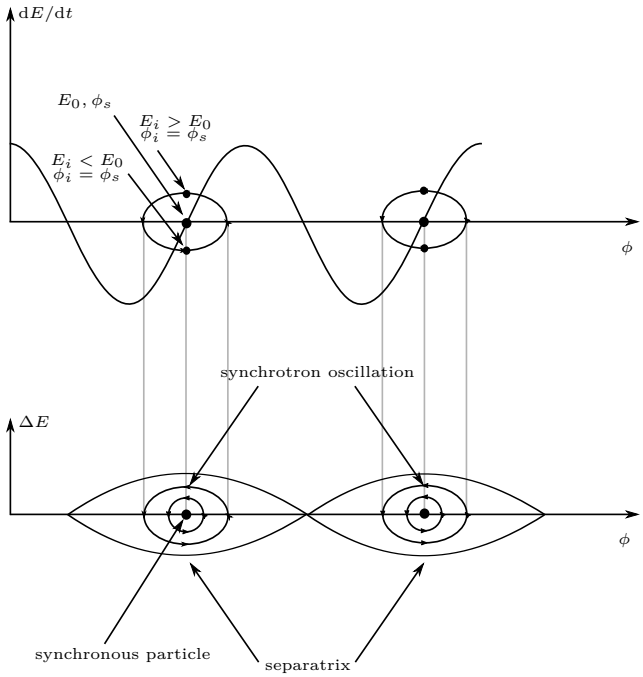

Figure 4.7: Bunching of the ion beam by the application of an RF voltage signal with $f_{RF} = 2f_0$ to a dedicated drift tube electrode. The phase and energy dependent energy gain $\mathrm{d}E/\mathrm{d}t$ in the resonator (top) leads to longituinal synchrotron oscillations (bottom) on a closed orbit resulting in a bunched ion beam with two bunches filling the circumference of the storage ring.

particles with frequency $f_s = f_0$ and phase ϕ_s have the exact energy E_0 to pass the RF electrode always at the exact same phase of the RF signal and thus experience no energy gain from the RF signal. However, particles with different energy E_i will pass the RF electrode earlier or later than the synchronous particle. A higher energetic particle $E_i > E_0$ with phase $\phi_i = \phi_s$ (shown in Figure 4.7, top), will, after one revolution, pass the RF electrode earlier than the synchronous particle and thus sees a smaller energy gain, vice versa for a low energetic particle $E_i < E_0$. Thus the energy difference between the particles, $\Delta E = E_i - E_0$, is reduced until $\Delta E = 0$ with $\Delta\phi = \phi_i - \phi_0$ then being maximal. Now, the processes is reversed. This results in an oscillation on a stable closed orbit in the longitudinal phase space (shown in Figure 4.7), i.e. *synchrotron oscillation* with the equation of motion [Hin08]

$$\frac{\mathrm{d}^2}{\mathrm{d}t^2}\Delta\phi + \omega_{sync}^2\Delta\phi = 0, \tag{4.2}$$

where $f_{sync} = \omega_{sync}/2\pi$ is the *synchrotron frequency*. The *separatrix* in Figure 4.7 indicates the border line between the stable and unstable area, i.e. the maximal phase $\Delta\phi$ and energy difference ΔE of a particle to still oscillate on the closed orbit. The enclosed stable area is called *bucket*. At the conditions in Figure 4.7, the ion beam is longitudinally redistributed to form two ion bunches. The bunches can fill a large part of the bucket. For simplicity, we describe the longitudinal intensity distribution in the storage ring by a $\cos^2 t$ function. Such bunched structured ion beam induces a strong signal on pickup electrodes [Vog16], which is easy to further process and acquire. A FOURIER transform of this signal would under our assumption give two delta peaks in frequency space at $f = 0$ and $f = 2f_0$.

In an RF-bunched ion beam with additional electron cooling, ions with a non-zero longitudinal velocity spread Δv (energy deviation ΔE) with respect to the synchronous particle experience a cooling force that compresses the occupied phase space area. This is shown by the red line in Figure 4.8. This results in a transformed time structure of the bunched ion beam, represented by two peaked profiles, each being narrower than the original $\sim \cos^2 t$ shapes (further discussed in subsection 4.2.2). Observations of this signal in frequency domain show emerging peaks at higher orders of the revolution frequency. Thus, we use the signal of the second harmonic of the RF signal as a sensitive probe for longitudinal electron cooling.

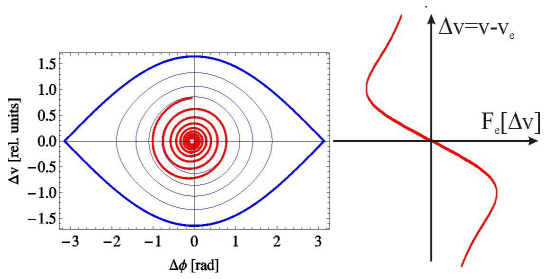

Figure 4.8: Longitudinal phase space compression by the electron cooling force. The left side shows the longitudinal phase space with the separatrix and the closed orbits. The energy deviation ΔE directly translates to a velocity spread Δv from the synchronous particle. The longitudinal cooling force, shown on the right side, compresses the occupied phase space area, indicated by the red lines. Image courtesy of M.Grieser.

We expect that the process of electron cooling becomes evident when observing an increasing signal at this frequency, i.e. $4f_0$. This measurement procedure is schematically shown in Figure 4.9.

We optimized the position and angle of the electron beam with respect to the ion beam. This is done by beam position measurements with the help of rotating wire scanners in the Ecool's straight section ([Loh15]) and electron beam manipulation by the application of transverse and vertical magnetic fields, i.e. steering the electron beam. For finer adjustments, we tuned the electron-ion interaction energy by carefully scanning the cathode voltage. This was done with having the RF bunching on all the time but in order to clearly identify the effect of electron cooling on the second harmonic signal, we switch on the electron beam 3 s after injection.

The strongest cooling effect was observed for the cathode voltage $U_0 = -43.58\,\mathrm{V}$ with an magnetic expansion factor of $\alpha = 20$ (subsection 3.2.3) and an electron current of $I = 14.4\,\mu\mathrm{A}$, shown in Figure 4.10. With optimal electron cooler settings the electron cooling was demonstrated by an increase of the signal at $4f_0$ right after switching on the electron beam. After some time the cooling reaches an equilibrium. As discussed in subsection 4.2.2, we find that this equilibrium represents the ion space charge limited mode where the effective RF force ($\mathrm{d}E/\mathrm{d}t$ in Figure 4.7) equals the space charge induced forces. Finally, we observe a decaying signal due to

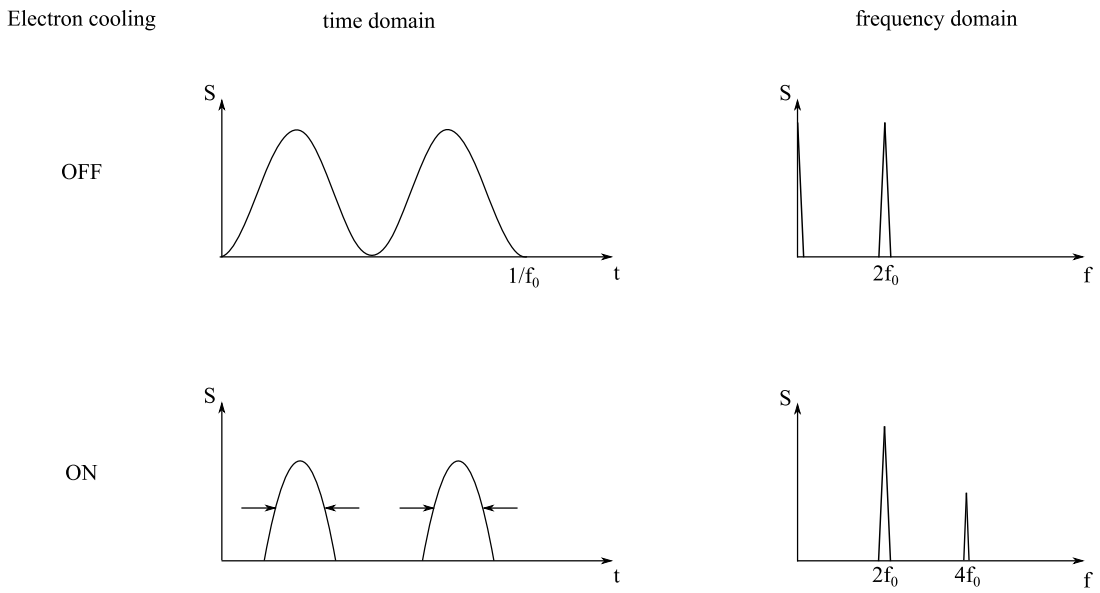

Figure 4.9: Pickup signal in time and frequency domain for the RF-bunched ion beam (top) and for the RF-bunched + electron cooled ion beam (bottom).

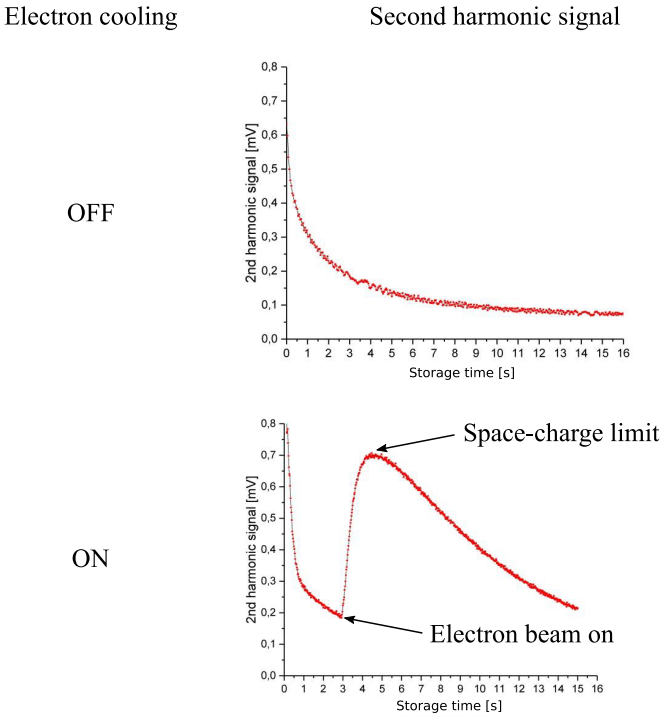

Figure 4.10: Temporal evolution of the current pick up signal at the second harmonic of the RF frequency $4f_0$ with and without electron cooling. Note, that the electron beam is switched on after 3 s.

the loss of ions which could not be understood in detail in these initial studies.

These observations demonstrate the first longitudinal electron cooling at the CSR electron cooler.

With the cathode potential $U_0 = -43.58\,\mathrm{V}$ in Figure 4.10 and the theoretically expected cooling energy for F^{6+} of $E_{cool} = 40.28\,\mathrm{eV}$, we can make an estimate on the contact potentials of the electrodes in the electron beam line. With the magnetic expansion of $\alpha = 20$ and an electron current of $I = 14.4\,\mu\mathrm{A}$, the space charge potential of the electron beam in the electron-ion interaction region can be calculated to be $U_{sc} = 0.18\,\mathrm{V}$ [KHS+92]. With Equation 4.1, we get the difference of contact potential to be $W_c - W_a = -3.12\,\mathrm{eV}$.

4.2.2 Longitudinal Ion beam profile in space charge limited mode

In order to investigate the ion space charge limit, we consider one bunch in the time domain that is recorded after reaching the equilibrium of electron cooling in Figure 4.10.

The longitudinal space charge field seen by an ion at longitudinal position s in the bunch (with $s = 0$ at the synchronous particle) with charge line density $\lambda(s)$ (seen in Figure 4.11) is calculated in [ES93] to be

$$E_{\parallel}(s) = -\frac{1 + 2\ln\left(\frac{R}{r}\right)}{4\pi\epsilon_0\gamma^2}\frac{\partial\lambda(s)}{\partial s}. \tag{4.3}$$

Here, ϵ_0 is the vacuum permittivity and γ is the relativistic mass increase (for the CSR, we set $\gamma = 1$). R is the beam tube radius while r is the average beam radius. A parabolic charge line density

$$\lambda(s) = \frac{3N_B Q}{4w_s}\left(1 - \frac{s^2}{w_s^2}\right), \tag{4.4}$$

with the number of ions per bunch N_B with ion charge Q and w_s representing the

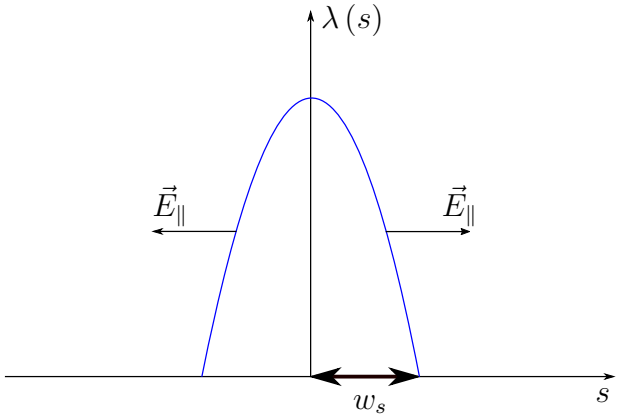

Figure 4.11: Theoretical model of an ion bunch in position space. The figure shows the parabolic charge line density $\lambda(s)$ for an electron cooled particle bunch versus longitudinal position s with bunch length w_s and the space charge field $\vec{E}_{\parallel}$.

bunch length in meters, shown in Figure 4.11, can be seen from Equation 4.3 to yield a longitudinal space charge field directly proportional to the phase difference $\Delta\phi$ ($s = -C_0\Delta\phi/2\pi h$) from the synchronous particle, i.e.

$$E_{\parallel}^{\text{sp.c.}} = -\frac{1+2\ln\left(\frac{R}{r}\right)}{4\pi\epsilon_0\gamma^2}\frac{3N_BQ}{4w_s^3}\frac{2C_0\Delta\phi}{2\pi h}. \tag{4.5}$$

Because of the relatively slow synchrotron oscillation with respect to one revolution in the ring, the longitudinal electric field, seen by an ion, can be assumed to be constant during one turn. Therefore, one can define an effective space charge voltage $U^{\text{sp.c.}} = E_{\parallel}^{\text{sp.c.}} \cdot C_0$. At the same time, the accelerating voltage of a particle with small $\Delta\phi$ ($\Delta\phi \ll \pi$) in the resonator (RF electrode) can be given by

$$U^{\text{acc}} = U\Delta\phi, \tag{4.6}$$

where U is the RF voltage. It is thus possible to reach an equilibrium where the energy gain in the resonator is compensated by the space charge voltage for all particles in the bunch, i.e. $U^{\text{sp.c.}} + U^{\text{acc}} = 0$. The bunch length in this equilibrium is

$$w_s = v_s C_0 \sqrt[3]{\frac{3\left(1+2\ln\left(\frac{R}{r}\right)\right)I}{2^4\pi^2c^4\epsilon_0\gamma^2h^2\beta^4U}}. \tag{4.7}$$

Here, $I = N_BQhv_s/C_0$ is the beam intensity, h the harmonic number and β the

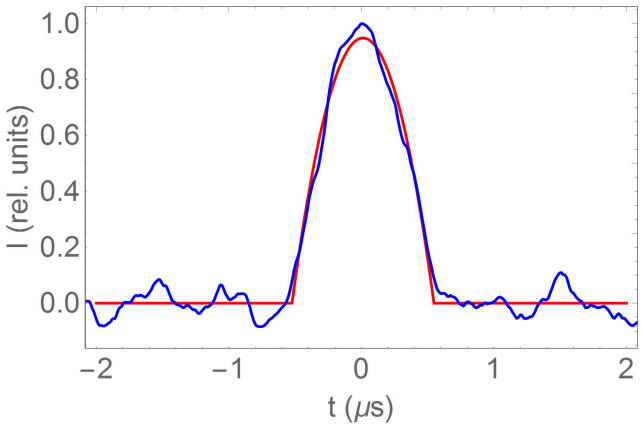

Figure 4.12: Fitted parabola of the charge line density $\lambda(t)$ and normalized experimental data of an ion bunch in the time domain.

beam velocity in units of speed of light c. Note that v_s is the velocity of the synchronous particle.

In the absence of electron cooling, the equilibrium in Equation 4.6 is unstable. Bunching by the resonator voltage leads to a larger space charge field which itself causes an expanding bunch size. This again lowers the space charge field which is making the energy gain from the resonator dominant. The ions start to oscillate. In the presence of electron cooling, the cooling force damps this oscillation producing a stable equilibrium where no synchrotron oscillation occurs. To verify whether we cooled down to this space charge limit, we test if our bunch distribution can be fitted by Equation 4.4.

Indeed, Figure 4.12 shows a satisfactory fit. Converting $s = v_s t$, we use the time scale and obtain a bunch time $w_{\mathrm{exp},s}/v_s = 535\,\mathrm{ns}$. Using the parameters of Table A.1, we obtain $w_{\mathrm{theo},s}/v_s = 597.5\,\mathrm{ns}$ which is close to our experimental result. This allows us to conlcude that we compress the ion bunch in longitudinal phase space down to the ion space charge limit.

5 Betatron oscillation tracking from detector position scans of a C_2^- ion beam

In subsection 2.1.3, it was discussed that the transversal motion of ions in a storage ring can be described by betatron oscillations about the design orbit. In the CSR, this oscillation can be demonstrated by a transversal oscillation of the ion beam limiting the quality of the beam for high precision collision experiments. Especially in merged-beam experiments it is advantageous to minimize the amplitude of the betatron oscillation in order to obtain a small dispersion in the interaction region.

The amplitude of the betatron oscillation gives a measure for the occupied phase space area, i.e. emittance, of the ion beam. A mismatch of the design orbit in the storage ring and the injected ion beam trajectory increases the attained phase space area causing large betatron oscillations (see Figure 2.3). In this section, we describe a novel method for the determination of the betatron oscillation amplitude which is in turn used for optimizing the trajectory of the injected ion beam.

In order to determine the betatron oscillation amplitude, one benefits from the fact that the ions are coherent when being injected into the CSR, i.e. all ions in each injection have approximately the same phase of the betatron oscillation. On short storage times, the coherence demonstrates as a phase space oscillation of the ion beam for each revolution. As a result also reaction products from such fluctuating beam appear to oscillate which can be projected onto the transverse position of the beam when impacting the detector. As further demonstrated in section 5.2 and section 5.3, a storage-time resolved position scan for the reaction products thus provides an information on the betatron oscillation phases for each ion beam revolution and therefore also on the betatron oscillation amplitude.

The specific implementation of this method using a C_2^- beam, specified in section 5.1,

and the COMPACT detector (subsection 2.2.3) is described in the following.

5.1 The C_2^- beam

We investigate the symmetric carbon dimer C_2^- with mass 24 u. The anions are produced from a metal ion sputter source (see subsection 2.2.2) and mass selected prior to the injection into the storage ring. We operated the platform voltage and ion optics such that a C_2^- beam with 60 keV kinetic energy is stored in the cryogenic ring with vacuum chamber wall temperatures far below 10 K. The ion source was optimized for a maximum current and we succeeded to store $\sim 2 \cdot 10^8$ ions in the ring. The number of ions was calculated from a measurement at the current pick-up electrode. During operation of the ion beam it was possible to tune the intensity of the injected ion beam. This was done by changing the focusing of the beam on the ion production platform in combination with a variable aperture.

Storing the C_2^- beam in absence of further reactants, e.g. photons, electrons or neutrals, allows us to observe two main decay channels:

$$C_2^- \rightarrow C_2 + e^-, \tag{5.1}$$

$$C_2^- \rightarrow C + C^-. \tag{5.2}$$

These are *autodetachment* and *autofragmentation*, respectively. The first occurs through *autoionization* [Fan61]. The latter results from delayed dissociation of the molecule where metastable quasibound vibrational states decay through the effective angular momentum barrier [FHAH05]. Due to a continuum of metastable states, one observes a continuum of decay constants leading to an autofragmentation signal which is represented by a power law decay versus storage time.

5.2 Betatron oscillation measurement

We measure with the COMPACT detector placed such that it collects neutral products (see subsection 2.2.3). Therefore, we observe both decay channels that are introduced in the previous section. Our data acquisition system allows us to count

the impact events with high storage-time resolution. The statistical quality of the data was improved by integrating over a number of injection cycles.

neutral beam profile

We perform measurements on the geometrical profile of the neutral product beam by moving the detector position through the beam line, i.e. scanning the cross section of the beam. For each position, we accumulate data from 40 injection cycles with 1 s total storage time and 1 µs storage time bin size. The beam intensity was adjusted such that we obtain at maximum $\sim$ 110 counts per injection so that the COMPACT detector is not saturated even at the very short storage times [SBF+15]. With this, we record data at 18 COMPACT positions spaced by 4 mm. The beam is now injected for 10 µs such that we see distinguishable bunches for each revolution. From this, we can get the revolution time to be 50.7731 µs. With this, we assign the storage time dependent count rate signal of the detector to individual revolutions for each detector position such that we get the turn-by-turn evolution of the transverse neutral beam profile. This is shown in Figure 5.1. Figure 5.1a shows the neutral beam profile normalized to the total number of counts for each revolution integrated over all positions. The normalized count rate is plotted against the COMPACT position. A gaussian fitting to every profile gives access to the mean peak position which itself is shown in Figure 5.1b. From Figure 5.1, we see a strong oscillation of the mean neutral beam profile position and additionally a large offset of the average mean profile position (57.0 mm) from the theoretically expected value of 36 mm (subsection 2.2.3). These observations suggest that the CSR's closed orbit was slightly displaced from the ideal orbit and thus also did not match the injected beam.

In order to match the closed orbit in the storage ring to the injected ion beam trajectory, it was necessary to optimize the ring's ion optics in order to obtain a larger orbit and thus shifting the neutral beam position further to the expected neutral product position of the detector. This was done by performing a closed orbit correction, i.e. scaling all CSR ion optic voltages to 0.99 of the initial values. After the correction, the revolution time of 50.8328 µs has been reached. The resulting neutral beam profiles are shown in Figure 5.2. Here, we see a smaller amplitude

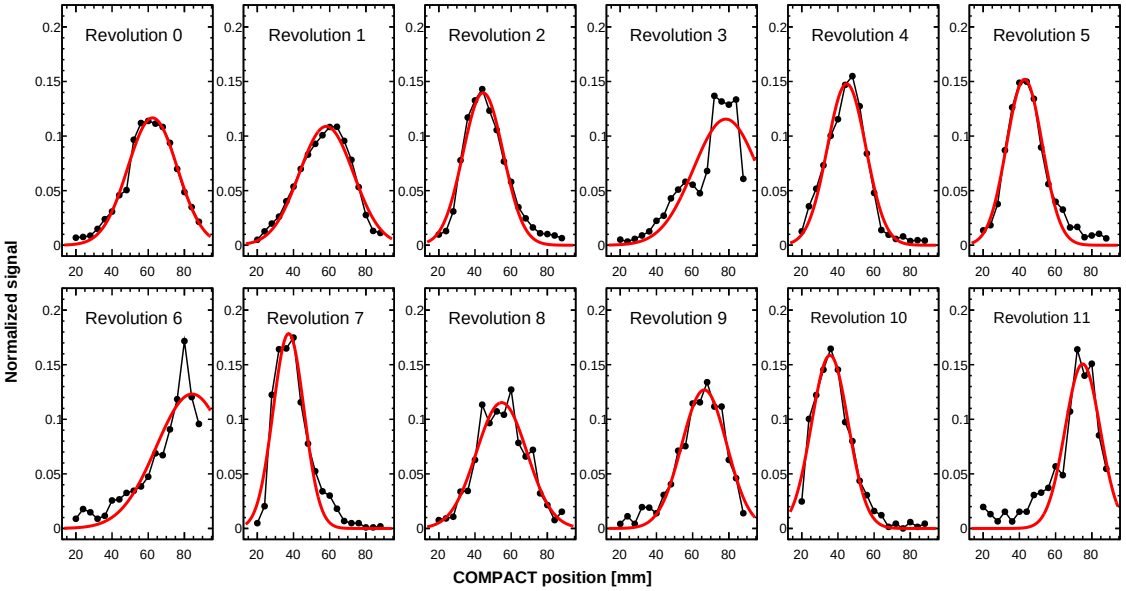

(a) Neutral beam profile of the first 12 revolutions.

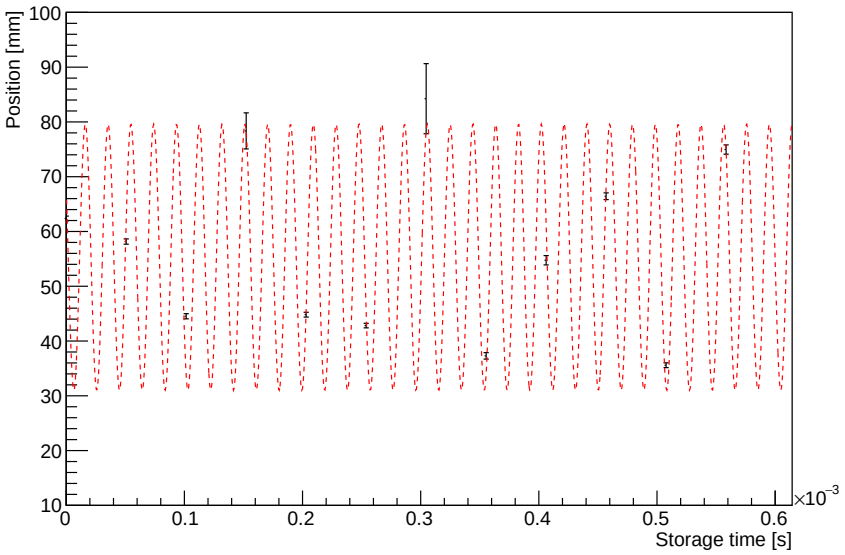

(b) Points with errorbars: Mean profile position against storage time for the first 12 revolutions. The dashed red lines indicate a plotted betatron oscillation function (discussed in section 5.3).

Figure 5.1: Temporal evolution of the neutral beam profile

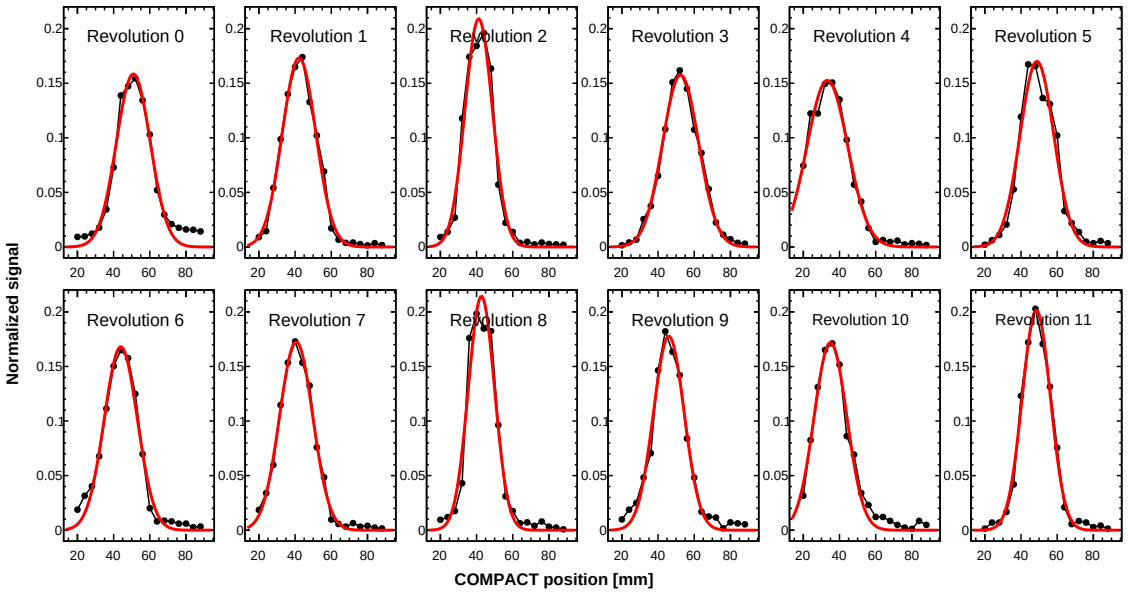

(a) Neutral beam profile of the first 12 revolutions, after closed orbit correction.

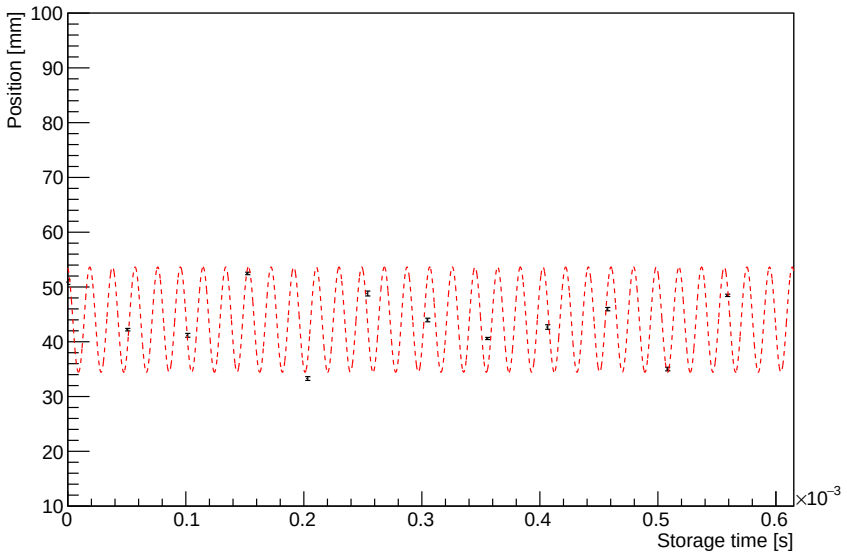

(b) Points with errorbars: Mean profile position against storage time for the first 12 revolutions, after closed orbit correction. The dashed red lines indicate a plotted betatron oscillation function (discussed in section 5.3).

Figure 5.2: Temporal evolution of the neutral beam profile after closed orbit correction by scaling to 0.99 of initial CSR ion optic voltages.

of the occurrent oscillation and a shift of the average mean profile position (now 43.8 mm) towards the expected value of 36 mm. We assume that the oscillation of the mean profile position comes from betatron oscillations in the storage ring (subsection 2.1.3), which will be shown in the following section.

5.3 Betatron oscillations

In subsection 2.1.3, it was shown that the transversal motion of the ion beam in a storage ring is governed by the betatron oscillations. This shall now be investigated for the horizontal degree of freedom (accessible by the COMPACT movement) by analyzing the results from section 5.2.

From Equation 2.17, we want to show that the temporal evolution of the horizontal mean profile position $X(t)$ in Figure 5.1 and Figure 5.2 follows

$$X(t) = X_{\text{off}} + A_x \cos(2\pi Q_x f_0 t + \phi). \tag{5.3}$$

Here, X_{off} is the offset position of the neutral beam and A_x is the horizontal amplitude of the betatron oscillation. Q_x is the horizontal tune (Equation 2.20) and ϕ is an offset phase.

Based on this expression, we perform an empirical fitting to the experimental data. This was done by calculating the PEARSON'S χ^2 value according to

$$\chi^2 = \sum_k \left(\frac{X_k - X(t_k)}{\Delta X_k} \right)^2, \tag{5.4}$$

where the sum is over the number of revolutions (position profiles), i.e. 12 in Figure 5.1 and Figure 5.2. X_k indicates the mean profile position and t_k the time at the kth revolution. ΔX_k in the denominator gives a weighting by the statistical uncertainties from the gaussian fitting of the profiles.

From the measured data (Figure 5.1b,Figure 5.2b), we can calculate the offset X_{off} and the amplitude A_x for both data sets. This is given in Table 5.1.

Data set	X_{off}[mm]	A_x[mm]
Before closed orbit shift	57.0	24.3
After closed orbit shift	43.8	9.6

Table 5.1: Calculated parameters from data sets in Figure 5.1 and Figure 5.2.

Data set	$Q_{x,1}$	ϕ_1	$Q_{x,2}$	ϕ_2
Before closed orbit shift	2.63	0.95	2.37	5.23
After closed orbit shift	2.64	0.25	2.35	6.03

Table 5.2: Q_x and ϕ values at the minimas observed in Figure 5.3.

In order to investigate the fitting of the betatron oscillation model in Equation 5.3 to our data, we calculate χ^2 from Equation 5.4 with fixed X_{off} and A_x in Equation 5.3 while varying both tune Q_x and offset phase ϕ from 2.2 to 2.8 and from 0 to 2π respectively. From this, we get a visual investigation of the χ^2 behaviour allowing us to identify local minima.

It should be noted that only the non-integer part q_x of the tune is experimentally accessible such that it is convenient to write

$$Q_x = m_x \pm q_x, \tag{5.5}$$

where m_x is the integer value and q_x is the fractional part of the tune. From measurements and simulations in [Vog16], we know that $q_x = 0.59$ and $m_x = 2$ with the working point of the CSR being $Q_x = 2.59$. However, it is experimentally not possible to differ between $Q_x = 2.41$ and $Q_x = 2.59$ (symmetric between two subsequent integer parts of the tune, here 2.5).

Figure 5.3 shows the logarithmic reduced χ^2 value $\log_{10}(\chi^2/\mu)$, where μ denotes the number of degrees of freedom, i.e. $\mu = 10$ with 12 measured profiles and two free parameters (Q_x and ϕ). The mapping is done for both data sets, i.e. before and after the closed orbit shift. In both Figure 5.3a and Figure 5.3b, we see two minima at the (Q_x, ϕ) pairs shown in Table 5.2. The observed results of Q_x comply with the theoretically expected values. As presumed, we observe two best fit minima repre-

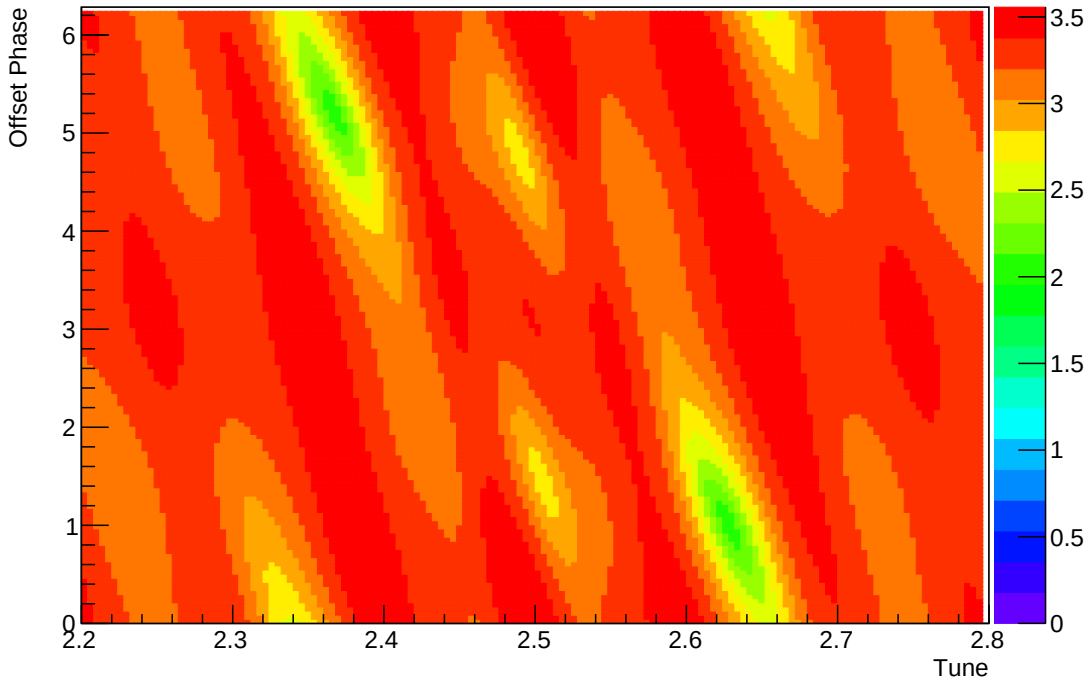

(a) $\log_{10}(\chi^2/\mu)$ before closed orbit correction.

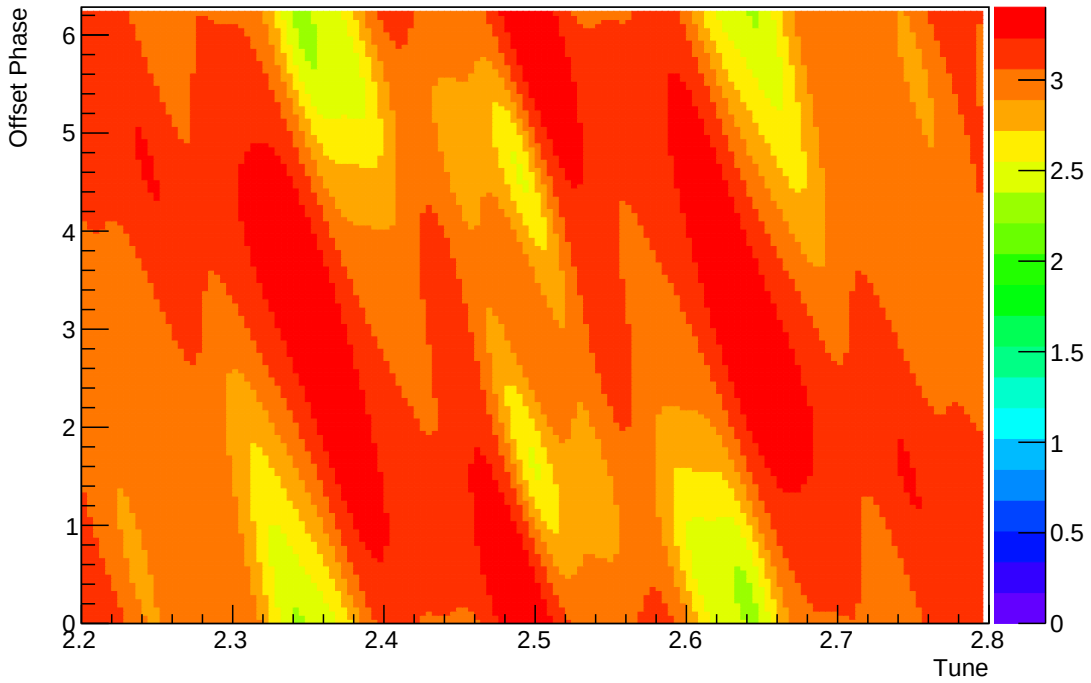

(b) $\log_{10}(\chi^2/\mu)$ after closed orbit correction.

Figure 5.3: Mapping of the $\log_{10}(\chi^2/\mu)$ versus varying tune and offset phase.

senting the two undistinguishable values of $Q_x = 2.41$ and $Q_x = 2.59$. This allows to conclude that the studied oscillation of the neutral product beam can indeed be described by betatron oscillations although the neutral product beam oscillations are a combination of angular and position effects of the parent beam in the long straight section upstream the detector, and the horizontal betatron oscillation model relies on the ideal conditions of a monoenergetic beam (see subsection 2.1.3).

For further visualization of the betatron oscillations of the mean neutral beam profile position, $Q_{x,1}$ and ϕ_1 from Table 5.2 were taken to plot Equation 5.3 with Table 5.1 to the datasets in Figure 5.1b and Figure 5.2b.

5.4 Discussion

From studies on the neutral beam mean profile position it was shown that the temporal evolution of these measurements can be represented by the horizontal betatron oscillations in the storage ring. This was done by empirically fitting the betatron oscillation model to the experimental data. The oscillation occurs with the expected tune value. By scaling the CSR voltages, a closed orbit shift was performed which allowed to reduce the amplitude of the occurring betatron oscillation. We assume that this comes from an improved overlap of the closed orbit with the injected beam. Simultaneous observation of the betatron oscillation and tuning of the CSR ion optics thus makes it possible to optimize the quality of the stored ion beam. This is in particular important when performing merged-beam experiments, i.e. electron cooling. Here, one aims for a small dispersion that facilitates the adjustment of the electron cooler.

6 Conclusion and Outlook

During the finalization of text of this thesis, it was possible to demonstrate longitudinal phase space cooling via electron cooling of a bunched F^{6+} ion beam for the first time at an electrostatic storage ring. The first operation of the CSR electron cooler is documented within this thesis and additionally the bunch length of an electron cooled ion bunch at the CSR was derived corresponding well to the theoretical model and thus demonstrating phase space cooling in the ion space charge limit.

Prior to this much effort was put into the implementation of the CSR Electron cooler focusing on the completion of the associated operational system.

Entirely controlling the kinematics of the electron beam over the electron beam line requires appropriate electrostatic beam optics. In order to perform electron cooling in an ion storage ring it is vital to precisely match the velocities of the merged-beams. Therefore, one main challenge to the operational system was to accurately tune the electron energy in the electron-ion interaction region. In addition, experiments with variable electron-ion collision energies shall be carried out while simultaneously benefiting from the advantageous properties of an electron-cooled, low-emittance ion beam. This work brought forth the manufacturing of a high-voltage platform serving as a versatile tool for a fully controlled operation of the CSR Electron cooler. Its design enables fast computer controlled operation at various electron-ion interaction energies. The Ecool high-voltage platform employs a multichannel power supply unit that is providing potentials to most electrodes in the electron beam line. Its concept and design is described in this thesis.

Operating the CSR electron cooler at the Cryogenic Storage Ring CSR is based on the interplay between these machines. Understanding the ion beam dynamics in the CSR is thus tremendously important when performing merged-beam experiments

with electrons. Therefore, investigations on the horizontal betatron oscillations in the CSR have been performed. This was done by observations of the neutral beam profile of C_2 molecules coming from autodetachment of C_2^- ions in the ring. It was shown that the oscillation of the mean neutral profile position comes from betatron oscillations in the storage ring. With this, it was possible to reduce the mismatch of the closed orbit of the storage ring and the injected beam, i.e. lowering the betatron oscillation amplitude. In the ongoing beam time (spring/summer 2017) of the CSR, these observations led to a new correction procedure prior to experiments with new ion species.

With this, two important contributions were made in order to reliably operate the Cryogenic Storage Ring CSR with electron-cooled ion beams. The basic operational system of the CSR electron cooler was finished and first cooling experiments have been performed. For future beam times, this system can be equipped with additional devices, i.e. the drift tube amplifiers for low electron energy operation, which was conceptionally presented in this thesis. The minimization of the betatron oscillation amplitude in the CSR was shown which will, in future beam times, also be performed by observations of the betatron sideband frequencies on the current pick up signal.

For future beam times, it is aimed to exploit the full potential of the CSR electron cooler in terms of experimental studies on dissociative recombination in a laboratory system mimicking interstellar conditions. This will be based on the knowledge and success of the first cryogenic electron cooling performance at an electrostatic storage ring performed during the work on this thesis.

A Appendix

A.1 Parameters of the electron cooled F^{6+} ion beam

Mass M	17.7 GeV
Kinetic energy E_{kin}	1.395 MeV
Beam velocity β	$\sqrt{\frac{2E_{kin}}{Me}} = 0.012\,508\,6\,\mathrm{c}$
harmonic number h	2
Resonator length L_0	0.35 m
CSR circumference C_0	35.1 m
Beam tube radius R	0.05 m
Beam radius r	3 mm
Beam intensity I	112 nA
Resonator voltage U_d	3.25 V
Absolute resonator voltage U	$\lvert 2U_d \sin\left(\frac{hL_0\pi}{C_0}\right)\rvert = 0.406\,977\,\mathrm{V}$

Table A.1: Parmeters of the F^{6+} beam for Equation 4.7.

A.2 Layout of the Multichannel power supply unit

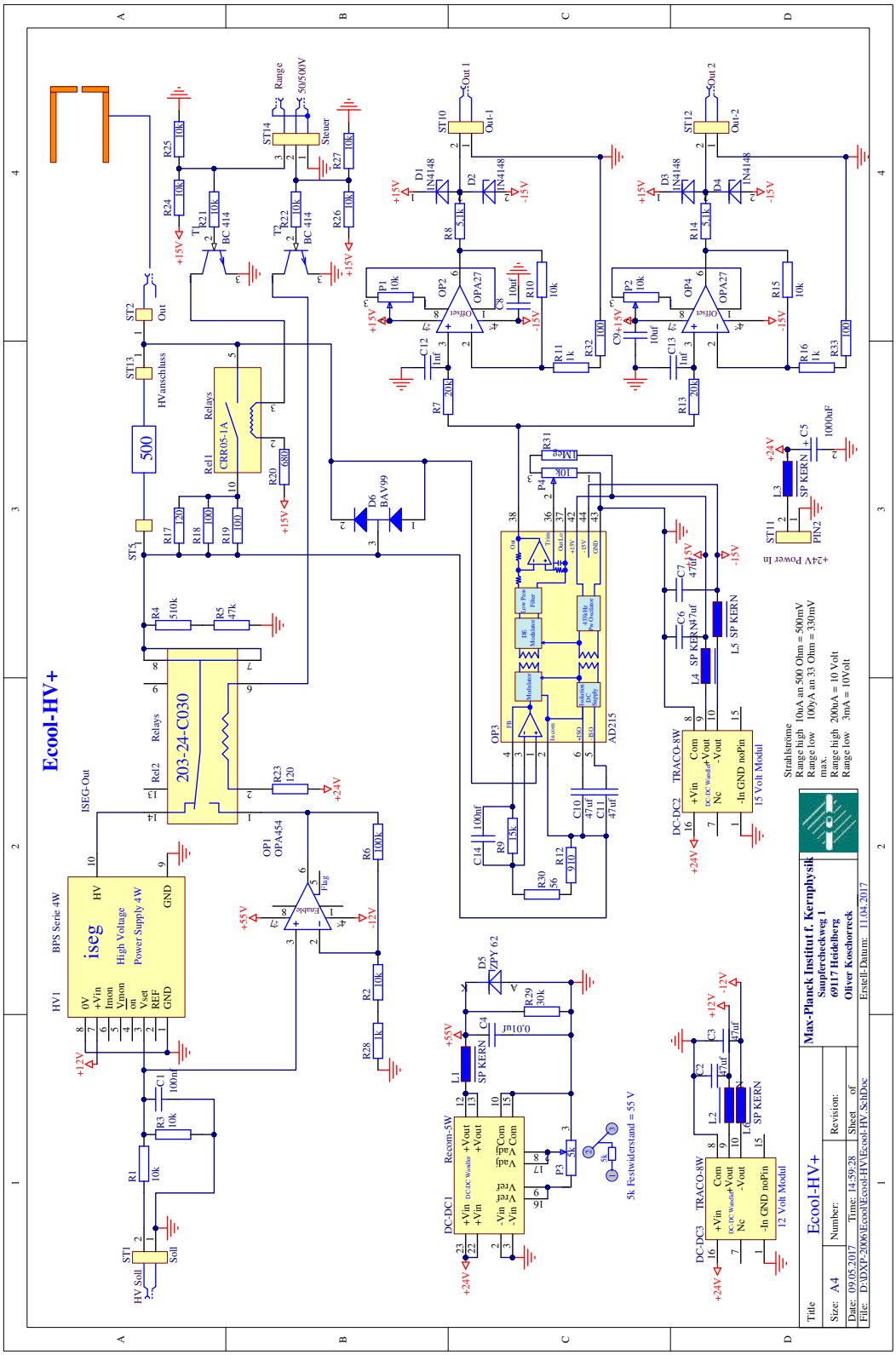

Figure A.1: Logics of a precise power supply unit of the Power supply & current measurement box. Image courtesy of O.Koschorreck

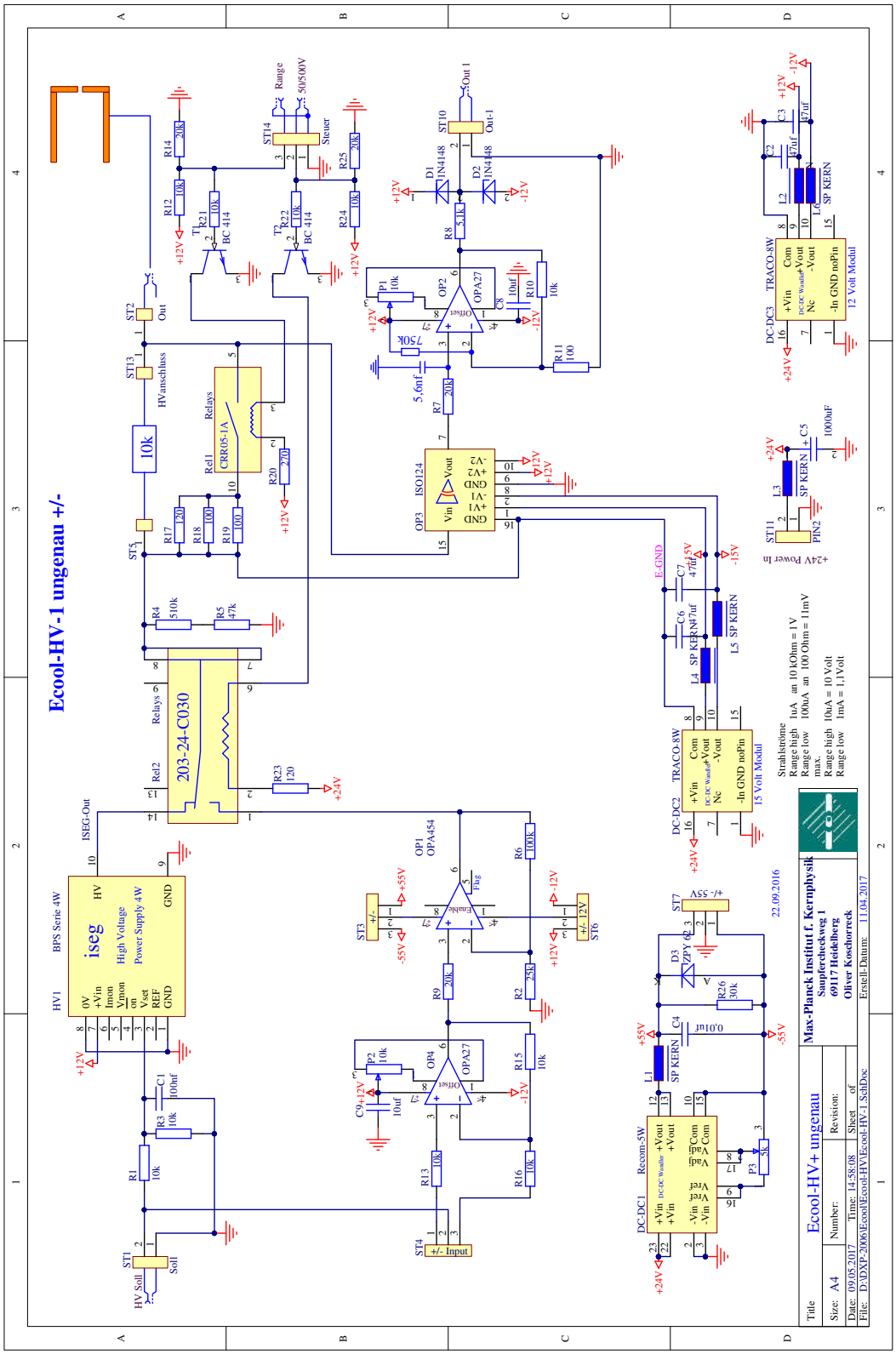

Figure A.2: Logics of a regular power supply unit of the Power supply & current measurement box. Image courtesy of O.Koschorreck

B Bibliography

[AG81] J. Arianer and R. Geller. The advanced positive heavy ion sources. *Ann. Nucl. Part. Sci.*, 31, 1981.

[Bec16] Arno Becker. *Imaging of Neutral Fragmentation Products from Fast Molecular Ion Beams: Paving the Way for Reaction Studies in Cryogenic Environment*. PhD thesis, 2016.

[BS78] G. I. Budker and Skrinskii. Electron cooling and new possibilities in elementary particle physics. *Sov. Phys. Usp.*, (21):277–296, 1978.

[Col06] LHCf Collaboration. LHC Design Report. *CERN*, 2006.

[CW32] J.D. Cockcroft and E.T.S. Walton. Experiments with high velocity positive ions. *Proc. Roy. Soc. (London)*, A136:619, 1932.

[Dan93] H. Danared. Fast electron cooling with a magnetically expanded electron beam. *Nuclear Inst. and Methods in Physics Research, A*, 335(3):397–401, 1993.

[DS78] Ya. S. Derbenev and A. N. Skrinsky. The effect of an accompanying magnetic field on electron cooling. *Particle Accelerators*, 8:235–243, 1978.

[ES93] D. A. Edwards and M.J. Syphers. *An Introduction to the Physics of High Energy Accelerators*. Wiley-Interscience Publication, 1993.

[Fan61] U. Fano. Effects of Configuration Interaction on Intensities and Phase Shifts. *Physical Review*, 124(6):1866, 1961.

[FHAH05] J. Fedor, K. Hansen, J.U. Andersen, and P. Hvelplund. Nonthermal Power Law Decay of Metal Dimer Anions. *Physical Review Letters*, 94(113201), 2005.

[Gol86] E. Goldstein. Ueber eine noch nicht untersuchte Strahlungsform an der Kathode inducirter Entladungen. *Monatsberichte der Königl. Akad. der Wiss. zu Berlin*, page 284, 1886.

[Gru16] Florian Grussie. *Experimental studies of ion-neutral reactions under astrophysical conditions*. PhD thesis, 2016.

[Hil86] G.W. Hill. On the part of the motion of the lunar perigee which is a function of the mean motions of the sun and moon. *Acta Mathematica*, 8(1):1–36, 1886.

[Hin08] Frank Hinterberger. *Physik der Teilchenbeschleuniger und Ionenoptik*, volume 2. 2008.

[HvD09] E. Herbst and E.F. van Dishoeck. Complex Organic Interstellar Molecules. *Annual Review of Astronomy and Astrophysics*, 47(1):427–480, 2009.

[Ker41] D.W. Kerst. The Acceleration of Electrons by Magnetic Induction. *Physical Review*, 60:47–53, 1941.

[KHS+92] G. Kilgus, D. Habs, D. Schwalm, A. Wolf, N. R. Badnell, and A. Müller. High-resolution measurement of dielectronic recombination of lithium-like Cu26+. *Physical Review A*, 46(9):5730, 1992.

[Kra09] Claude Krantz. *Intense Electron Beams from GaAs Photocathodes as a Tool for Molecular and Atomic Physics*. PhD thesis, 2009.

[KT73] N. Krall and A. Trivelpiece. *Principles of plasma physics*. Mc Graw-Hill Inc., 1973.

[Lar97] M. Larsson. Dissociative recombination with ion storage rings. *Annual Review of physical chemistry*, 48:151–179, 1997.

[LE30] E.O. Lawrence and N.E. Edlefsen. Sur la production de protons de grande vitesse. *Science*, 72:376, 1930.

[Len94] P. Lenard. Ueber Kathodenstrahlen in Gasen von atmosphärischem Druck und im äussersten Vacuum. *Annalen der Physik und Chemie*, 51:225, 1894.

[Lio15] Jorrit Lion. *Das mit Flüssigneon gekühlte supraleitende Magnetsystem des Elektronenkühlers am kryogenenen Ionen-Speicherring CSR*. Bachelor thesis, Universität Heidelberg, 2015.

[LO08] M. Larsson and A. E. Orel. *Dissociative Recombination of Molecular Ions*. Cambridge University Press, 2008.

[Loh15] Svenja Lohmann. *Beam diagnostics and collector for the electron cooler of the cryogenic storage ring CSR*. Master thesis, Universität Heidelberg, 2015.

[McM45] E.M. McMillan. The Synchrotron—A Proposed High Energy Particle Accelerator. *Physical Review*, 68:143, 1945.

[Mül99] A. Müller. Plasma rate coefficients for highly charged ion-electron collisions: new experimental access via ion storage rings. *International Journal of Mass Spectrometry*, 192:9–22, 1999.

[OAT00] D. Orlov, V. E. Andreev, and A. S. Terekhov. Elastic and Inelastic Tunneling of Photoelectrons from Dimensional Quantization Band at a p+ - GaAs-(Cs,O) Interface into Vacuum. *JETP Lett.*, 71:151, 2000.

[OWS+04] D. Orlov, Udo Weigel, D. Schwalm, A. S. Terekhov, and A. Wolf. Ultracold Electron Source with a GaAs-Photocathode. *Nuclear Inst. and Methods in Physics Research, A*, 532:418, 2004.

[Per15] A.L. Peratt. *Physics of the Plasma Universe*. 2015.

[PHDM99] R. A. Phaneuf, C. C. Havener, G. H. Dunn, and A. Müller. Merged-beams experiments in atomic and molecular physics. *Reports on Progress in Physics*, 62:1143, 1999.

[Pot90] Helmut Poth. Electron cooling: Theory, experiment, application. *Physics Reports*, 196(3-4):135–297, 1990.

[PSG+96] S. Pastuszka, U. Schramm, M. Grieser, C. Broude, R. Grimm, D. Habs, J. Kenntner, H. J. Miesner, T. Schüßler, D. Schwalm, and A. Wolf. Electron cooling and recombination experiments with an adiabatically

expanded electron beam. *Nuclear Instruments and Methods in Physics Research, Section A: Accelerators, Spectrometers, Detectors and Associated Equipment*, 369(1):11–22, 1996.

[Rut11] E. Rutherford. The scattering of α and β particles by matter and the structure of the atom. *Phil. Mag.*, 21:669, 1911.

[SBF+15] Kaija Spruck, Arno Becker, Florian Fellenberger, Manfred Grieser, Robert Von Hahn, Vincent Klinkhamer, Old??ich Novotn??, Stefan Schippers, Stephen Vogel, Andreas Wolf, and Claude Krantz. An efficient, movable single-particle detector for use in cryogenic ultra-high vacuum environments. *Review of Scientific Instruments*, 86(2), 2015.

[Sho12] Andrey Shornikov. *An electron cooler for ultra-low energy cryogenic operation.* PhD thesis, 2012.

[Spi62] L. Spitzer. Physics of Fully Ionized Gases. *Wiley, New York*, 2nd ed., 1962.

[Spr03] Frank Sprenger. *Production of cold electron beams for collision experiments with stored ions.* PhD thesis, 2003.

[Spr15] Kaija Spruck. *Dielectronic Recombination Experiments with Tungsten Ions at the Test Storage Ring and Development of a Single-Particle Detector at the Cryogenic Storage Ring.* PhD thesis, 2015.

[SvL65] J.J. Scheer and J. van Laar. GaAs-Cs: A New Type of Photoemitter. *Solid State Commun.*, 3(8):189–193, 1965.

[VBB+16] R. Von Hahn, A. Becker, F. Berg, K. Blaum, C. Breitenfeldt, H. Fadil, F. Fellenberger, M. Froese, S. George, J. Göck, M. Grieser, F. Grussie, E. A. Guerin, O. Heber, P. Herwig, J. Karthein, C. Krantz, H. Kreckel, M. Lange, F. Laux, S. Lohmann, S. Menk, C. Meyer, P. M. Mishra, O. Novotny, A. P. O'Connor, D. A. Orlov, M. L. Rappaport, R. Repnow, S. Saurabh, S. Schippers, C. D. Schröter, D. Schwalm, L. Schweikhard, T. Sieber, A. Shornikov, K. Spruck, S. Sunil Kumar, J. Ullrich, X. Urbain, S. Vogel, P. Wilhelm, A. Wolf, and D. Zajfman. The cryogenic storage ring CSR. *Review of Scientific Instruments*, 87(6), 2016.

[Vek44] V.I. Veksler. A new method of relativistic particle acceleration. *Proc. USSR Acad. Sci.*, 43:346, 1944.

[Vog16] Stephen Vogel. *Developments at an Electrostatic Cryogenic Storage Ring for Electron-Cooled keV Energy Ion Beams.* PhD thesis, 2016.

[Wei03] Udo Weigel. *Cold intense electron beams from Gallium Arsenide photocathodes.* PhD thesis, 2003.

[WHG+06] A. Wolf, R. Von Hahn, M. Grieser, D. Orlov, H. Fadil, C. Welsch, V. Andrianarijaona, A. Diehl, C. Schroter, and J. C. Lopez-Urrutia. The Heidelberg CSR: Stored ion beams in a cryogenic environment. *AIP Conference Proceedings*, 821(IOP Publishing):473, 2006.

[Wid28] R. Wideröe. On a New Principle to Generate High Voltages. *Archiv für Elektrotechnik*, 21:387, 1928.

[Wol92] Andreas Wolf. *Wechselwirkung zwischen hochgeladenen Ionen und freien Elektronen in einem Ionenspeicherring: dynamische Reibung und Rekombination.* Professorial dissertation, 1992.

Erklärung:

Ich versichere, dass ich diese Arbeit selbstständig verfasst habe und keine anderen als die angegebenen Quellen und Hilfsmittel benutzt habe.

Heidelberg, den 26.06.2017 .....